

# Is there really a Black Hole at the center of NGC 4041? - Constraints from gas kinematics<sup>1</sup>

A. Marconi<sup>2</sup>, D.J. Axon<sup>3</sup>, A. Capetti<sup>4</sup>, W. Maciejewski<sup>2,11</sup>, J. Atkinson<sup>3</sup>, D. Batcheldor<sup>3</sup>,  
J. Binney<sup>6</sup>, M. Carollo<sup>7</sup>, L. Dressel<sup>5</sup>, H. Ford<sup>8</sup>, J. Gerssen<sup>5</sup>, M.A. Hughes<sup>3</sup>, D. Macchetto<sup>5,9</sup>,  
M.R. Merrifield<sup>10</sup>, C. Scarlata<sup>5</sup>, W. Sparks<sup>5</sup>, M. Stiavelli<sup>5</sup>, Z. Tsvetanov<sup>8</sup>,  
R.P. van der Marel<sup>5</sup>

## ABSTRACT

We present HST/STIS spectra of the Sbc spiral galaxy NGC 4041 which were used to map the velocity field of the gas in its nuclear region. We detect the presence of a compact ( $r \simeq 0''.4 \simeq 40$  pc), high surface brightness, rotating nuclear disk co-spatial with a nuclear star cluster. The disk is characterized by a rotation curve with a peak to peak amplitude of  $\sim 40 \text{ km s}^{-1}$  and is systematically blueshifted by  $\sim 10\text{--}20 \text{ km s}^{-1}$  with respect to the galaxy systemic velocity. With the standard assumption of constant mass-to-light ratio and with the nuclear disk inclination taken from the outer disk, we find that a dark point mass of  $(1^{+0.6}_{-0.7}) \times 10^7 M_{\odot}$  is needed to reproduce the observed rotation curve. However the observed blueshift suggests the possibility that the nuclear disk could be dynamically decoupled. Following this line of reasoning we relax the standard assumptions and find that the kinematical data can be accounted for by the stellar mass provided that either the central mass-to-light ratio is increased by a factor of  $\sim 2$  or that the inclination is allowed to vary. This model results in a  $3\sigma$  upper limit of  $6 \times 10^6 M_{\odot}$  on the mass of any nuclear black hole. Overall, our analysis only allows us to set an upper limit of  $2 \times 10^7 M_{\odot}$  on the mass of the nuclear BH. If this upper limit is taken in conjunction with an estimated bulge B magnitude of  $-17.7$  and with a central stellar velocity dispersion of  $\simeq 95 \text{ km s}^{-1}$ , then these results are not inconsistent with both the  $M_{\text{BH}}\text{--}L_{\text{sph}}$  and the  $M_{\text{BH}}\text{--}\sigma_{\star}$  correlations. Constraints on BH masses in spiral galaxies of types as late as Sbc are still very scarce and therefore the present result adds an important new datapoint to our understanding of BH demography.

*Subject headings:* black hole physics — galaxies: individual (NGC 4041) — galaxies: kinematics and dynamics — galaxies: nuclei — galaxies: spiral

<sup>1</sup>Based on observations made with the NASA/ESA Hubble Space Telescope, obtained at the Space Telescope Science Institute, which is operated by the Association of Universities for Research in Astronomy, Inc., under NASA contract NAS 5-26555. These observations are associated with proposal #8228.

<sup>2</sup>INAF- Osservatorio Astrofisico di Arcetri, L.go Fermi 5, I-50125 Firenze, Italy

<sup>3</sup>Department of Physical Sciences, University of Hertfordshire, Hatfield AL10 9AB, UK

<sup>4</sup>INAF- Osservatorio Astronomico di Torino, Strada Osservatorio 20, 10025 Pino Torinese, Torino, Italy

<sup>5</sup>Space Telescope Science Institute, 3700 San Martin Drive, Baltimore, MD 21218

<sup>6</sup>Theoretical Physics, 1 Keble Road, Oxford OX1 3NP,

## 1. Introduction

It has long been suspected that the most luminous AGN are powered by accretion of mat-

UK

<sup>7</sup>Eidgenössische Technische Hochschule Zuerich, Henggerberg HPF G4.3, CH-8092 Zuerich, Switzerland

<sup>8</sup>Department of Physics and Astronomy, Johns Hopkins University, 3400 North Charles Street, Baltimore, MD 21218

<sup>9</sup>ESA Space Telescopes Division

<sup>10</sup>School of Physics & Astronomy, University of Nottingham, NG7 2RD, UK

<sup>11</sup>also, Obserwatorium Astronomiczne Uniwersytetu Jagiellońskiego, Poland

ter onto massive black holes (hereafter BH; e.g. Lynden-Bell 1969). This belief, combined with the observed evolution of the space-density of AGN (Soltan 1982; Chokshi & Turner 1992; Marconi & Salvati 2001) and the high incidence of low luminosity nuclear activity in nearby galaxies (Ho, Filippenko, & Sargent 1997), implies that a significant fraction of luminous galaxies must host black holes of mass  $10^6 - 10^{10} M_{\odot}$ .

It is now clear that a large fraction of hot spheroids (E-S0) contains a BH (Harms et al. 1994; Kormendy & Richstone 1995; Kormendy et al. 1996; Macchetto et al. 1997; van der Marel & van den Bosch 1998; Bower et al. 1998; Marconi et al. 2001) with mass proportional to the mass (or luminosity) of the host spheroid ( $M_{\text{BH}}/M_{\text{sph}} \approx 0.001$  e.g. Merritt & Ferrarese 2001). Recently Ferrarese & Merritt (2000) and Gebhardt et al. (2000) have shown that a tighter correlation holds between the BH mass and the velocity dispersion of the bulge. Clearly, any correlation of black hole and spheroid properties would have important implications for theories of galaxy formation in general, and bulge formation in particular. However, to date, there are very few secure BH measurements or upper limits in spiral galaxies even though we know that AGNs are common in such systems (Maiolino & Rieke 1995). In total, there are 37 *secure* BH detections according to Kormendy & Gebhardt (2001) or just 22 according to Merritt & Ferrarese (2002), depending on the definition of “secure”. Only  $\sim 20\%$  of these BH detections (7/37 or 4/22, respectively) are in galaxy types later than S0, and only 3 in Sbc’s and later (the Milky Way, Genzel et al. 2000; NGC 4258, Miyoshi et al. 1995; NGC 4945, Greenhill, Moran, & Herrnstein 1997). It is therefore important to directly establish how common are BHs in spiral galaxies and if they follow the same  $M_{\text{BH}}-M_{\text{sph}}$ ,  $M_{\text{BH}}-\sigma_{\star}$  correlations as Elliptical galaxies.

This can be achieved only with a comprehensive survey for BHs that covers quiescent and active spiral galaxies of all Hubble types. Such a survey would pin down the mass function and space density of BHs, and their connection with host galaxy properties (e.g., bulge mass, disk mass etc).

To detect BHs one requires spectral information at the highest possible angular resolution: the “sphere of influence” (Bahcall & Wolf 1976) of BHs are typically  $\leq 1''$  even in the most nearby

galaxies. Nuclear absorption-line spectra can be used to demonstrate the presence of a BH (Kormendy & Richstone 1995; Richstone 1998; van der Marel et al. 1998b), but the interpretation of the data is complex because it involves stellar-dynamical models that have many degrees of freedom – that can be pinned down only when data of very high S/N are available (Binney & Mamon 1982; Statler 1987; Merritt 1997; Binney & Merrifield 1998). Radio-frequency measurements of masers in disks around BHs provide some of the most spectacular evidence for BHs, but have the disadvantage that only a small fraction of the disks will be inclined such that their maser emission is directed toward us (Braatz, Wilson, & Henkel 1997). Studies of ordinary optical emission lines from gas disks provide an alternative and relatively simple method to detect BHs.

HST studies have discovered many cases of such gas disks in early-type galaxies (M87, Ford et al. 1994; NGC 4261, Jaffe et al. 1996; NGC 5322, Carollo et al. 1997; Cen A, Schreier et al. 1998) and have demonstrated that both their rotation curves and line profiles are consistent with thin disks in Keplerian motion (Ferrarese et al. 1996; Macchetto et al. 1997; Ford et al. 1998; van der Marel & van den Bosch 1998; Bower et al. 1998; Marconi et al. 2001).

In early-type galaxies there are still worrying issues about the dynamical configuration of nuclear gas (e.g., misalignment with the major axis, irregular structure etc). By contrast nuclear gas in relatively quiescent spirals is believed to be organized into well defined rotating disks seen in optical line images (e.g., M81, Devereux, Ford, & Jacoby 1997). Ho et al. (2002) recently found that the majority of spiral galaxies in their survey has irregular velocity fields in the nuclear gas, not well suited for kinematical analysis. Still, 25% of the galaxies where H $\alpha$  emission was detected all the way to the center have velocity curves consistent with circular rotation and the galaxies with more complicated velocity curves can also be useful for BH mass measurement after detailed analysis of the spectra. Indeed, even in the most powerful Seyfert nuclei such as NGC 4151, where the gas is known to be interacting with radio ejecta, it may be possible to get the mass of the BH from spatially resolved HST spectroscopy by careful analysis of the velocity field to separate the underlying

quiescently rotating disk gas from that disturbed by the jets (Winge et al. 1998).

Prompted by these considerations, we have undertaken a spectroscopic survey of 54 spirals using STIS on the Hubble Space Telescope. Our sample was extracted from a comprehensive ground-based study by Axon et al. who obtained  $H\alpha$  and  $[N II]$  rotation curves at a seeing-limited resolution of  $1''$ , of 128 Sb, SBb, Sc, and SBc spiral galaxies from RC3. By restricting ourselves to galaxies with recession velocities  $V < 2000$  km/s, we obtained a volume-limited sample of 54 spirals that are known to have nuclear gas disks and span wide ranges in bulge mass and concentration. The systemic velocity cut-off was chosen so that we can probe close to the nuclei of these galaxies, and detect even lower-mass black holes. The frequency of AGN in our sample is typical of that found in other surveys of nearby spirals, with comparable numbers of weak nuclear radio sources and LINERS. The sample is described in detail by Axon et al. (paper in preparation).

This paper presents the observations of NGC 4041, the first object observed, and a detailed description of the analysis and modeling techniques which will be applied to the other galaxies in the sample. From the Lyon/Meudon Extragalactic Database (LED<sup>12</sup>), NGC 4041 is classified as a Sbc spiral galaxy with no detected AGN activity. Its average heliocentric radial velocity from radio measurements is  $1227 \pm 9$  km s<sup>-1</sup> becoming  $\simeq 1480$  km s<sup>-1</sup> after correction for Local Group infall onto Virgo. With  $H_0 = 75$  km s<sup>-1</sup> Mpc<sup>-1</sup> this corresponds to a distance of  $\simeq 19.5$  Mpc and to a scale of 95 pc/''.

The outline of the paper is as follows. In §2 we present the adopted observational strategy and data reduction techniques. In §3 we present the rotation curves of the ionized gas and the broadband images of the nuclear region of the galaxy. In §4.1 we derive the stellar luminosity density from the observed surface brightness distribution which is then used in the model fitting of the kinematical data. All the details of the inversion procedure are described in Appendix A. The model fitting of the kinematical data is described in §4.2 and all the details of the model computation are described in Appendix B. In particular, §4.2.2 describes the

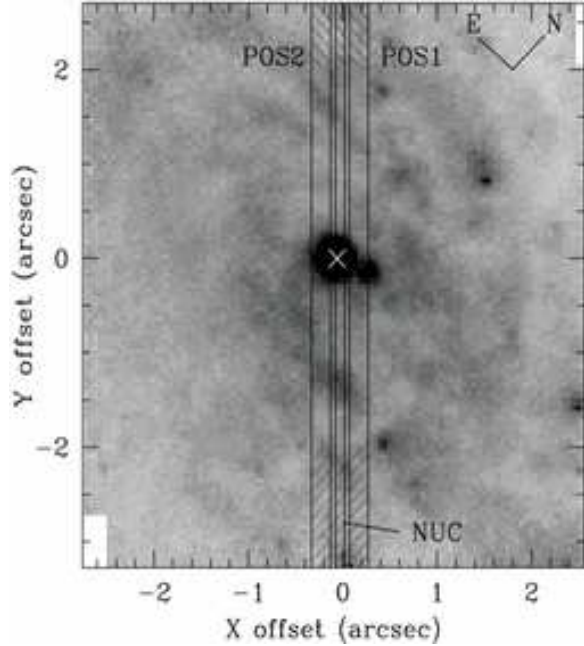


Fig. 1.— Slit positions overlaid on the acquisition image. The 0,0 position is the position of the target derived from the STIS ACQ procedure. The white cross is the kinematic center derived from the fitting of the rotation curves (see §4.2).

*standard* approach, while in §4.2.3 an *alternative* approach is considered. In §5 we discuss the effects of our assumptions on the derived value of the BH mass for which, in the present case, only an upper limit can be set. We then compare this upper limit with the  $M_{BH}$ - $L_{sph}$  and  $M_{BH}$ - $\sigma_*$  correlations. Finally, our conclusions are presented in §6.

## 2. Observations and Data Reduction

### 2.1. STIS observations

NGC 4041 was observed with STIS on the HST in 1999 July 7. An  $\sim 5'' \times 5''$  acquisition image was obtained with the F28X50LP filter and the galaxy nucleus, present within the field of view, was subsequently centered and re-imaged following the ACQ procedure. The exposure time of the acquisition images was 120 s.

The observational strategy consisted in obtaining spectra at three parallel positions with the central slit centered on the nucleus and the flanking ones at a distance of  $0''.2$ . The slit positions are

<sup>12</sup><http://leda.univ-lyon1.fr>

overlaid on the acquisition image in Figure 1 and their position angle is  $43^\circ$ . At each slit position we obtained two spectra with the G750M grating centered at  $H\alpha$ , with the second spectrum shifted along the slit by an integer number of detector pixels in order to remove cosmic-ray hits and hot pixels. The nuclear spectrum (NUC) was obtained with the  $0''.1$  slit and no binning of the detector pixels, yielding a spatial scale of  $0''.0507/\text{pix}$  along the slit, a dispersion per pixel of  $\Delta\lambda = 0.554 \text{ \AA}$  and a spectral resolution of  $\mathcal{R} = \lambda/(2\Delta\lambda) \simeq 6000$ . The off-nuclear spectra (POS1 and POS2) were obtained with the  $0''.2$  slit and  $2 \times 2$  on-chip binning of the detector pixels, yielding  $0''.101/\text{pix}$  along the slit,  $1.108 \text{ \AA}/\text{pix}$  along the dispersion direction and  $\mathcal{R} \simeq 3000$ . Total exposure times were 950 s for the NUC position and 420 s and 500 s for POS1 and POS2, respectively.

The acquisition images were flat-fielded, realigned and co-added in order to improve the signal-to-noise ratio. The pixel scale is  $0''.0507$ . The flux calibration was first obtained using the PHOTFLAM header in the image. We subsequently applied a color correction to convert to Johnson R magnitudes. In order to do this, we used the average spectra of Sb and Sc spiral galaxies from Kinney et al. (1996) as spectral templates.

The raw spectra were reprocessed through the *calstis* pipeline using the darks obtained daily for STIS. Standard pipeline tasks were used to obtain flat-field corrected images. The two exposures taken at a given slit position were then realigned with a shift along the slit direction (by an integer number of pixels) and the pipeline task *ocrreject* was used to reject cosmic rays and hot pixels. Subsequent calibration procedures followed the standard pipeline reduction described in the STIS Instrument Handbook (Leitherer et al. 2001), i.e. the spectra were wavelength calibrated and corrected for 2D distortions. The expected accuracy of the wavelength calibration is  $0.1 - 0.3 \text{ pix}$  within a single exposure and  $0.2 - 0.5 \text{ pix}$  among different exposures (Leitherer et al. 2001) which converts into  $\sim 3 - 8 \text{ km s}^{-1}$  (relative) and  $\sim 5 - 13 \text{ km s}^{-1}$  (absolute). The relative error on the wavelength calibration is negligible for the data presented here because our analysis is restricted to the small detector region including  $H\alpha$  and  $[\text{N II}]$  ( $\Delta\lambda < 100 \text{ \AA}$ ).

The nominal slit positions obtained as a result of the STIS ACQ procedure were checked by

matching the light profiles measured along the slit with the synthetic ones derived from the acquisition image: we collapsed the spectra along the dispersion direction and compared the resulting light profiles with the ones extracted from the acquisition image for a given slit position. The agreement is good for all slit positions and the center of the NUC slit is offset by only  $\sim 0''.03$  with respect to the position of the target determined by the STIS ACQ procedure (0,0 position in Figure 1).

We selected the spectral regions containing the lines of interest and subtracted the continuum by fitting a linear polynomial row by row along the dispersion direction. The continuum subtracted lines were then fitted row by row with gaussian functions using the task LONGSLIT in the TWODSPEC FIGARO package (Wilkins & Axon 1992) and the task *specfit* in the IRAF<sup>13</sup> *stdas* package. When the signal-to-noise ratio (SNR) was insufficient (faint line) the fitting was improved by co-adding two or more pixels along the slit direction.

## 2.2. WFPC2 images

WFPC2 images in the F450W ( $\sim B$ ), F606W ( $\sim R$ ) and F814W ( $\sim I$ ) filters were retrieved from the archive. These images encompass the entire galaxy with the nucleus located in the WF3 chip. The data were automatically reprocessed with the best calibration files available before retrieval. Two exposures were performed in each of the three filters, in order to remove cosmic rays. Warm pixels and cosmic rays were removed (STSDAS tasks *warmpix* and *crrej*) and mosaicked images with spatial sampling of  $0''.1/\text{pix}$  were obtained using the *wmosaic* task, which also corrects for the optical distortions in the four WFPC2 chips. The background was estimated from areas external to the galaxy where no emission is detected. Flux calibration to Vega magnitudes was performed using the zero points by Whitmore (1995). To convert to standard filters in the Johnson-Cousins system we estimated the color correction using various spectral templates, A0V and K0V stars and the Sb and Sc spiral spec-

<sup>13</sup>IRAF is distributed by the National Optical Astronomy Observatories, which are operated by the Association of Universities for Research in Astronomy, Inc., under cooperative agreement with the National Science Foundation.

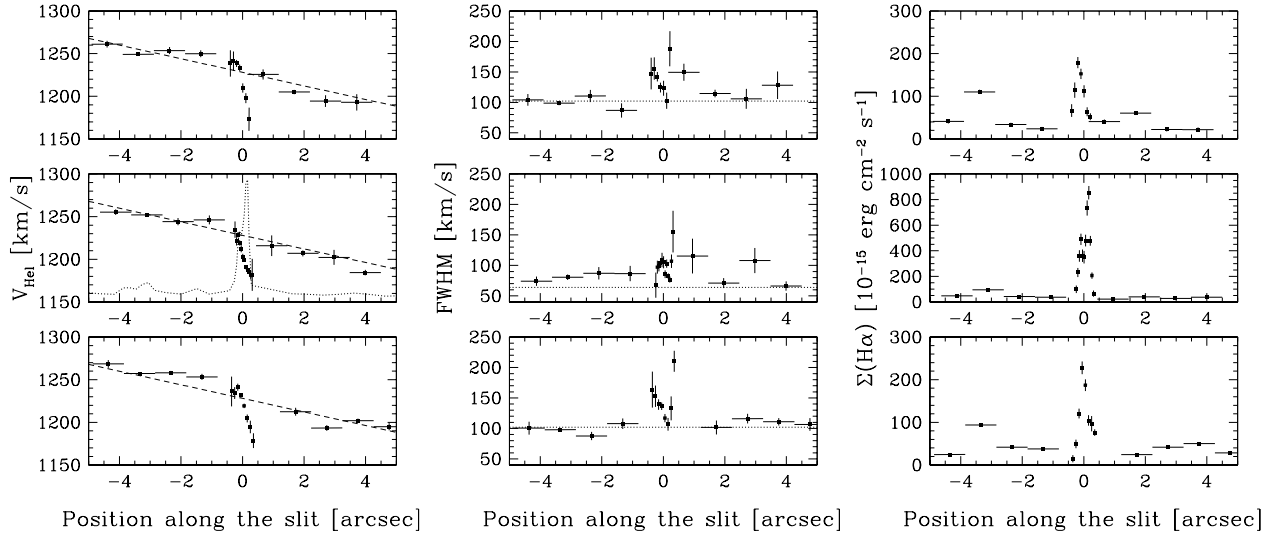


Fig. 2.— From left to right: velocity, FWHM and Surface brightness measured along the slit at POS1, NUC and POS2 (from top to bottom). Vertical bars are  $1\sigma$  errors while horizontal bars indicate the size of the aperture over which the quantity was measured. In the left panel, the dashed line is the velocity gradient measured in the ground based data. The dotted line in the NUC rotation curve panel is the line surface brightness along the slit, drawn in order to pinpoint the high surface brightness nuclear disk. The dotted lines in the FWHM panels corresponds to instrumental widths. The 0 position along the slit corresponds to the position of the nuclear continuum peak.

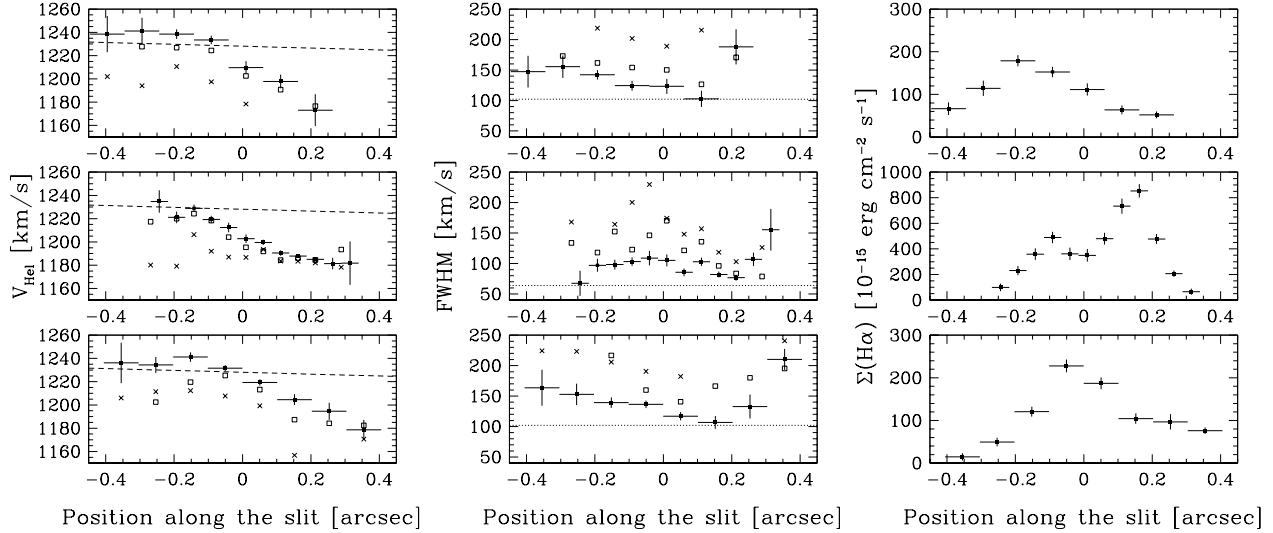


Fig. 3.— Same as previous figure but for the points related to the nuclear disk. The points with the errorbars are the quantities derived in the fit which takes into account the presence of the blue wing and in which H $\alpha$  and [N II] emitting media are constrained to have the same velocity and FWHM. Conversely the points without the errorbars are derived with unconstrained, single gaussian fits of H $\alpha$  (open square) and [N II] (crosses). For more details see §3.1.1.

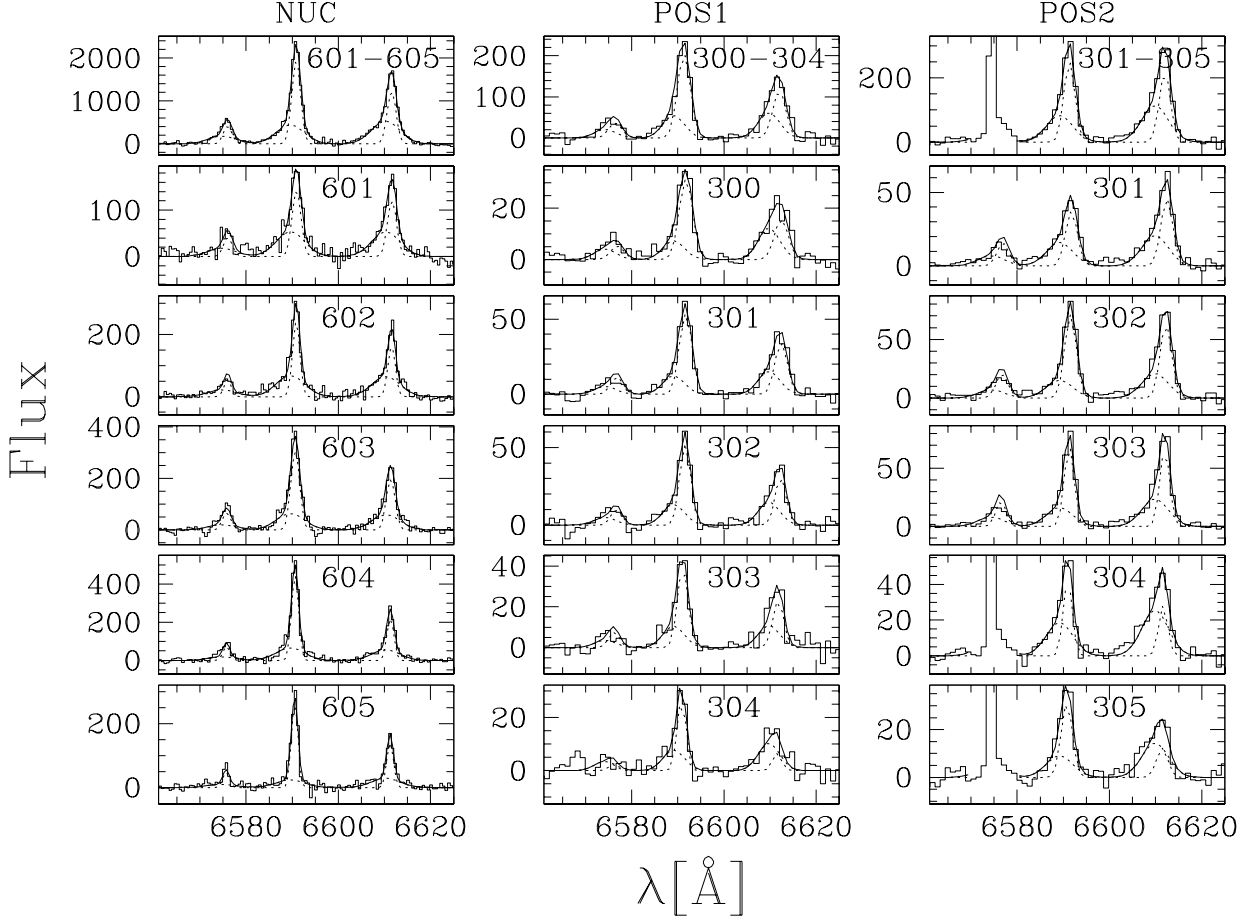


Fig. 4.— Fits of the line profiles at the three slit positions. The dotted lines identify the two components of the fit. Each component is characterized by the same velocity and FWHM for H $\alpha$  and [NII]. The ratio between the two [NII] lines is that fixed by atomic physics. At every slit position the blue component has the same velocity and width at each row and their values are determined in the fit of the overall nuclear spectrum shown in the upper panels. The numbers in the upper right corners of each panel are the row or the range of rows where the fit was performed. The strong narrow lines in the right panels are residual cosmic rays which have been excluded from the fit.

tra from Kinney et al. (1996). The color corrections are the following:  $I - F814W \simeq -0.1$  (Sb, K0V) and  $-0.005$  (A0V);  $R - F606W \simeq -0.4$  (Sb, K0V) and  $-0.05$  (Sc, A0V);  $B - F450W \simeq 0.1$  (Sb, K0V) and  $0.0$  (Sc, A0V). With these corrections, the differences between colors from Johnson-Cousins and HST instrumental magnitudes are  $\Delta(R - I) \simeq -0.3; -0.04$ ,  $\Delta(B - I) \simeq 0.2; 0.0$ ,  $\Delta(B - R) \simeq 0.5; 0.0$  according to the templates used. Unless stated otherwise, we have applied the color corrections derived from the K0V star and Sb spiral templates, which are most suitable

to the present data.

### 2.3. Ground based observations

NGC 4041 was also observed with NICS (Baffa et al. 2001) at the Telescopio Nazionale Galileo (TNG) in 2001 February 12 using the  $K'$  filter and the small field camera which yields a  $0''.13$  pixel size. The night was not photometric and seeing during the observations was  $\sim 0''.8$ . Observations consisted of several exposures, each with the object at a different position on the array. Data re-

duction consisted in flat-fielding and sky subtraction. The frames were then combined into a mosaic. In order to flux calibrate the NICS image we have used the 2MASS image available on the web. The 2MASS K band image is flux calibrated to an accuracy of  $< 0.1\text{mag}$  and has a spatial resolution of  $\sim 3''.5$  with a pixel size of  $1''$ . We have therefore degraded the spatial resolution of the NICS image to the 2MASS image and rebinned to  $1''$  pixels. We have performed ellipse fitting to both images and rescaled the NICS image to the flux calibrated 2MASS data by comparing the light profiles.

The NICS image and WFPC2 images were then realigned by cross correlating common features in the nuclear region, because no point sources are present in the near infrared image. The main feature which drives the correlation is the strong nuclear peak, however we have checked that, even excluding the central peak, the shift between the images can be determined with an accuracy of  $\pm 0''.2$  (i.e.  $\pm 2$  pixels of WFPC2) in both directions. With this accuracy the nuclear continuum peaks present in both optical and infrared images are consistent with being at the same position.

### 3. Results

#### 3.1. Kinematics

##### 3.1.1. Line fitting procedures

Line-of-sight velocities, full width at half maxima (hereafter FWHM) and surface brightnesses along each slit were obtained by fitting single gaussians to  $\text{H}\alpha$  and  $[\text{NII}]$  emission lines in each row of the continuum-subtracted 2D spectra. In the left panels of Figure 2 we plot the measured velocities. Beyond  $0''.5$  of the nucleus velocities show considerable small scale variations likely due to local gas motions which do not reflect the mass distribution. Therefore we averaged velocities by binning the spectra in steps of  $1''$  (10 rows in NUC and 5 in POS1,2), while, within  $0''.5$  of the nucleus velocities are measured along each row to take advantage of all the spatial information. Similarly, the central and right panels in Figure 2 display FWHMs and  $\text{H}\alpha$  surface brightnesses as measured along the slit.

In Figure 2, the dotted line superimposed on the NUC rotation curve represents the  $\text{H}\alpha$  surface brightness shown in the right central panel.

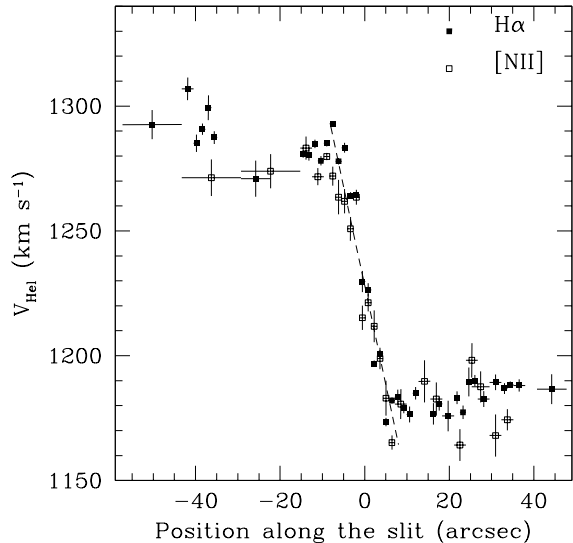


Fig. 5.— Ground based rotation curve obtained at  $\text{PA}=43^\circ$ . The dashed line is the constant velocity gradient from the solid body part of the rotation curve also shown in Figures 2 and 3.

This helps to distinguish the presence of two components: an extended one, characterized by a low surface brightness ( $< 10^{-13} \text{ erg cm}^{-2} \text{ s}^{-1} \text{ arcsec}^{-2}$ ), roughly constant along the slit, and nuclear one, compact (within  $-0''.4$  and  $0''.4$ ), bright and cospatial with the position of the nuclear continuum peak. This might be interpreted as a nuclear disk of the same extent as the nuclear stellar cluster described in §3.2. As shown in more detail in the right hand panel of Figure 3, the emission line surface brightness of the nuclear disk is double peaked while the nuclear continuum source, roughly coincident with the center of rotation, is located in-between the two peaks.

Fitting single unconstrained gaussians is acceptable for the extended component but it does not produce good results for the points in the nuclear region. In particular a single gaussian fit produces velocities of  $\text{H}\alpha$  and  $[\text{NII}]$  which differ by as much as  $\sim 30 - 40 \text{ km s}^{-1}$  (see Figure 3). This is not a worrisome issue if the amplitude of the rotation curve is a few  $100 \text{ km s}^{-1}$  but makes interpretation of the data uncertain in the present case where the amplitude of the nuclear rotation curve is only  $\sim 40 \text{ km s}^{-1}$ . A careful analysis of

the line profiles in the nuclear region shows that they are persistently asymmetric with the presence of a blue wing (see Figure 4).

A fit row by row with two gaussian components, the main component and the blue one, with the constraint that they have the same velocities and widths for  $H\alpha$  and  $[N II]$ , shows that, within the large uncertainties, the “blue wing” has always the same velocity and width. We have then deblended the “blue” component in the spectrum obtained by co-adding the central 5 rows. The velocity and width of the blue component were then used in the row by row fit. The constrained fit is good and  $H\alpha$  and  $[N II]$  now have the same velocity in the main component. The measured velocities, FWHMs and  $H\alpha$  surface brightnesses in the nuclear region are shown in Figure 3 where we also plot, as a comparison, the values obtained from unconstrained single gaussian fits of  $H\alpha$  and  $[N II]$ . Given the signal-to-noise of the present data, the nature of the blue wing is, as yet, unclear.

### 3.1.2. Velocity curves

The velocity field of the extended component shows a quasi-linear gradient of  $\sim 8 \text{ km s}^{-1}/''$  which agrees with the velocity gradient (Figure 5) measured from ground-based observations at the same PA as our STIS spectra (Axon et al., paper in preparation). The velocity gradient measured from the ground based rotation curve is shown as a straight line in the figures. The large scale trend observed from HST matches very well the expected gradient from the solid body part of the ground based rotation curve although it presents structures at small scales.

Within  $0''.5$  of the nucleus, the velocity field shows a smooth S-shaped curve with a peak to peak amplitude of only  $40 \text{ km s}^{-1}$  (left panel of Figure 3). Overall there is no hint of a steep Keplerian rise around a point-like mass.

The central velocities of the nuclear curves are systematically offset from the large scale velocity field by  $\sim 10 - 20 \text{ km s}^{-1}$  (compare with the dashed line which is the solid body part of the rotation curve - left panel of Figure 3). The off-nuclear slits show essentially the same velocity field as the on-nucleus slit. Thus this blueshift must be real and not an instrumental artifact generated by light entering the slit off center (for a

detailed discussion on the effects of light entering the slit off-center see Maciejewski & Binney 2001). For example, consider the case in which the peak of line emission is on the blue side (left on Figure 1) of the NUC slit. Then the measured velocity will be blueshifted with respect to the true value. The same would happen for POS1. However in POS2 the peak of the line emission will be on the red side of the slit and the measured velocities will be shifted to the red with respect to the true value. This is not the case for our data. The possible origin and implications of this blueshift are discussed in §5.

### 3.2. Morphology

The acquisition image, shown in Figure 1, has a field-of-view of  $5'' \times 5''$ . In Figure 6 we show the inner  $30'' \times 30''$  and  $5'' \times 5''$  of the WFPC2 and NICS images. Finally in Figure 7 we plot the color maps.

The acquisition image (Figure 1) shows a compact but resolved ( $\text{FWHM} \simeq 0''.2$ ) bright central feature superimposed to the central region of the bulge. A second bright feature is present  $\sim 0''.4$  SW of the nucleus. Figure 8 represents the radial light profile from the STIS acquisition image. As already clear from the acquisition image, the light profile indicates the presence of a bright central feature. This feature is spatially extended as can be seen from a comparison with the light profile of an unresolved source (NGC 4051) obtained with the same instrumental setup. This nuclear feature is likely to be a star cluster; a photometrically distinct star cluster is often present in the dynamical center of spiral galaxies of all Hubble types (e.g. Carollo, Stiavelli & Mack 1998; Carollo et al. 2002; Böker et al. 2002, and references therein).

The same central source is visible in all the WFPC2 images and an analysis of its colors (Figure 7) indicates that it is bluer than the surrounding regions but still redder than the galaxy disk and bulge. Its Vega magnitudes in the three WFPC2 filters are 19.10 (F450W), 18.05 (F606W) and 17.16 (F814W) with formal uncertainties of  $\pm 0.02 \text{ mag}$ . These values, converted to Johnson magnitudes, become  $B=19.2$ ,  $R=17.7$ ,  $I=17.1$  for the K0V and Sb spiral spectra and  $B=19.1$ ,  $R=18.0$ ,  $I=17.15$  for the A0V and Sc spiral spectra. The star cluster emission is very weak in the K band and not readily visible but its location is



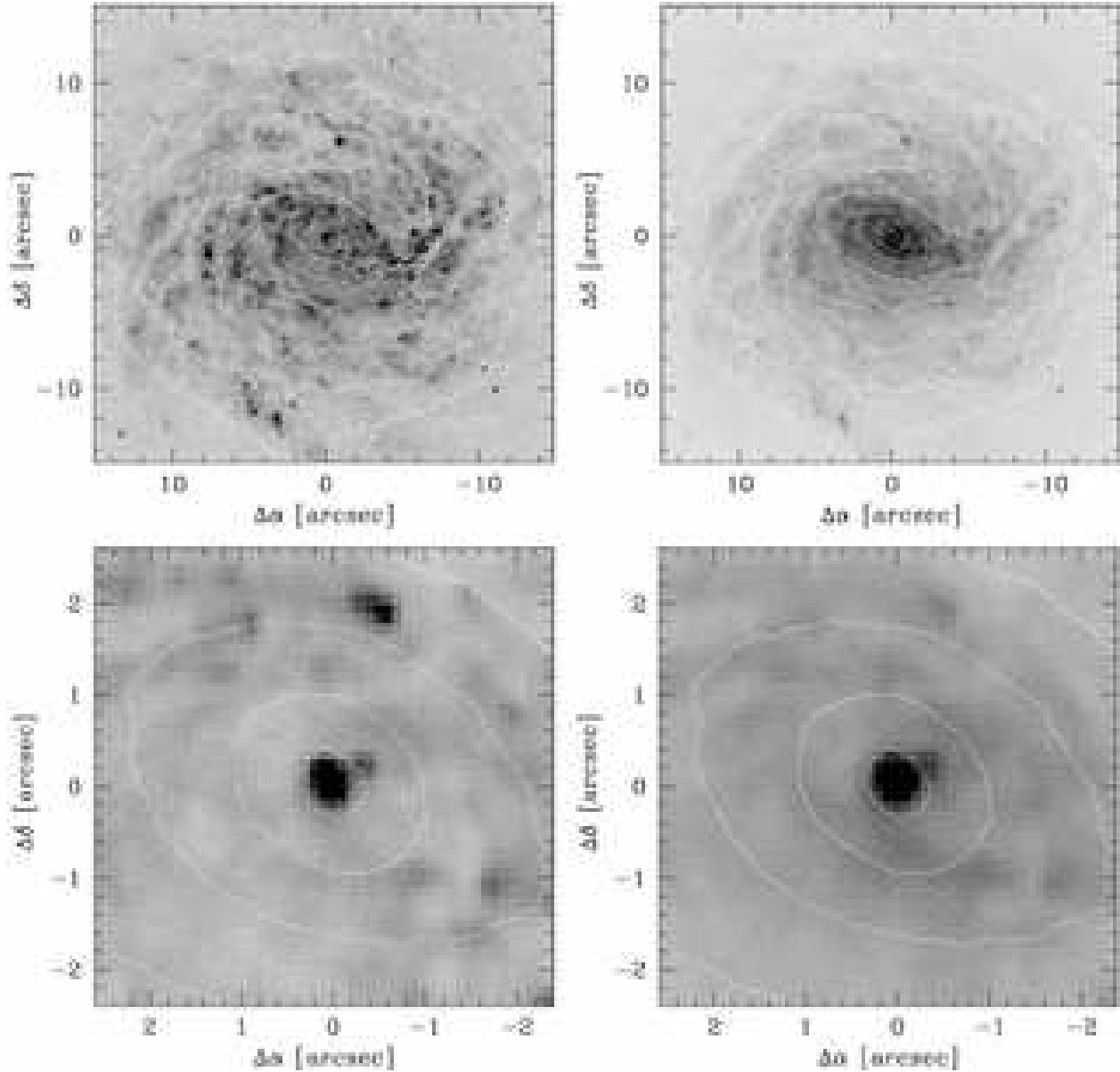


Fig. 6.— Overlay of the K band isophotes on the grayscale of the F450W (left) and F814W (right) WFPC2 images. North is up and East is left. The bottom panels show an expanded view of the nuclear region.

coincident with the location of the K band peak within the alignment uncertainties ( $\sim 0''.2$ , see Figure 6).

The color images show that the inner few arcseconds are redder than the galaxy disk and bulge and this could either be due to the presence of obscuration by dust or to a change in stellar population.

From several galaxy catalogues it can be inferred that the inclination of the large scale disk is  $\sim 20^\circ$ . This is supported by the nearly circular isophotes observed in the NICS and WFPC2 images at large scales  $> 20'' - 30''$ . However, in the inner regions, a bar-like structure is visible in the K band image oriented  $\sim$  E-W. It is extended for  $\sim 15''$  i.e.  $\sim 1.4$  kpc with isophotes symmetri-

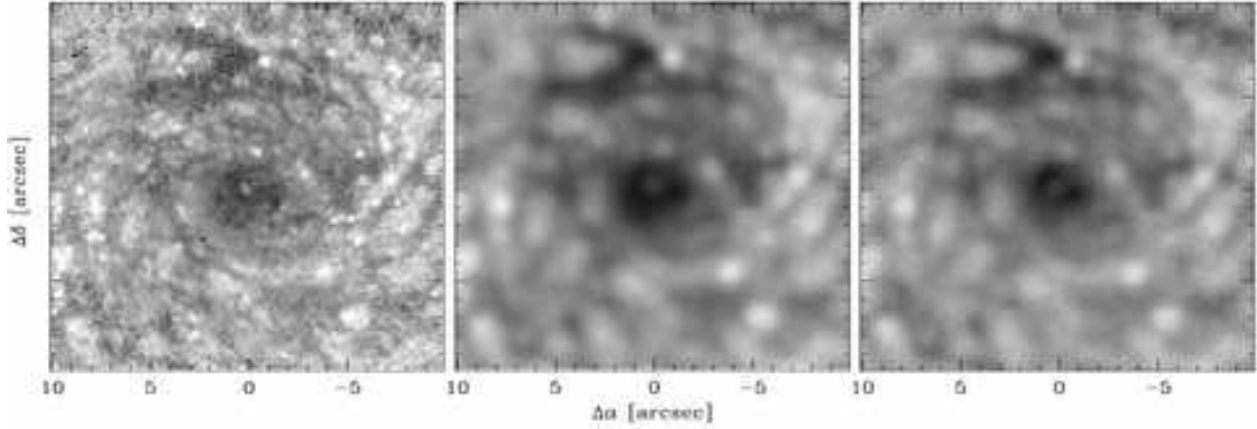


Fig. 7.—  $20'' \times 20''$  view of the color images of the central region of NGC 4041. The center of the images coincides with the location of the nucleus. North is up and East is left. From left to right:  $B - I$ ,  $B - I$  degraded to NICS resolution,  $B - K$  with  $B$  (from WFPC2/F450W) degraded to NICS resolution. The dark regions have redder colors.

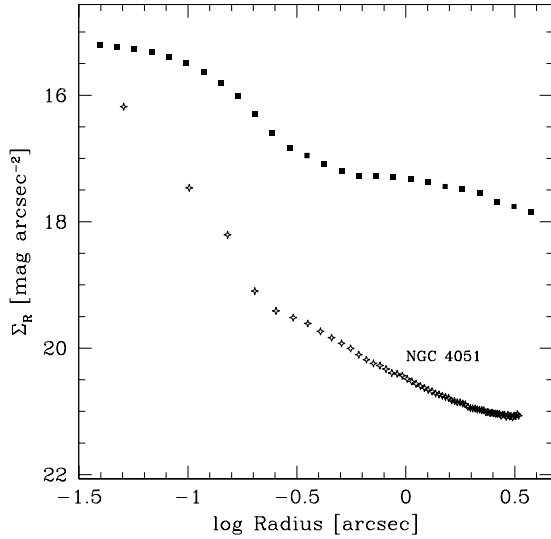


Fig. 8.— Radial light profile from the STIS acquisition image. The empty diamonds represent the radial light profile from a galaxy, NGC 4051, having a strong central unresolved source; the profile was rescaled to match the NGC 4041 one in the central pixel.

cally twisted on both ends. The twisting is most likely due to spiral arms just outside (and apparently connecting to) the bar. These give the bar

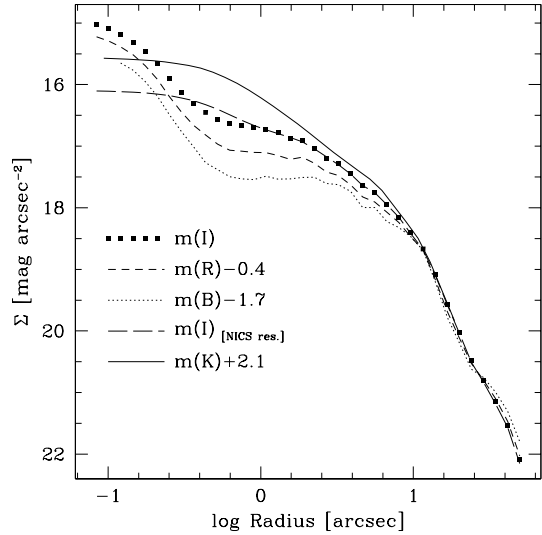


Fig. 9.— Azimuthally averaged light profiles for the WFPC2 and NICS images. All images have been rescaled to match the external light profile of the F814W image. The scaling factors applied are indicated in the figure and directly show the color in the outer regions where the profiles match. “NICS res.” indicates that the F814W image has been degraded to the NICS resolution.

the appearance of being larger than it is. It is well known (see, e.g. Shaw et al. 1995; Knapen et al. 1995) that strong concentrations of young stars can dominate the K-band. This likely happens in the region where spiral arms emanate from the bar in NGC 4041: blue-star complexes are seen in color images there, particularly at the west end (Figure 6). The bar itself is rather short with semi-major axis length at most  $\sim 3''$ , and a position angle of about  $60^\circ$ . It is a weak bar, given the fatness of the observed structure and that it is lacking the pair of dust lanes characteristic for strong bars (Athanasoula 1992). Instead, a mini-spiral structure is seen in the STIS ACQ image (Figure 1), extending at least out to  $3''$  from the nucleus, i.e. throughout the entire IR bar. Such a morphology indicates that we shouldn't expect strong departures from the circular motion in the gas flow. In fact, the CO velocity field observed by Sakamoto et al. (1999, see their Figure 1f) shows no such deviations down to the  $4''$  beam size of the observations. The PA of the kinematical line of nodes is  $\simeq 85^\circ$ , close to the PA of the bar.

### 3.2.1. Light Profiles

The canonical way to derive light profiles from images is to fit ellipses to the isophotes and to measure encircled fluxes. However, inspection of Figures 1 and 6 indicates the presence of small scale structures invalidating the ellipse fits of the WFPC2 and STIS images. The NICS image is much smoother but the ellipticity of its inner isophotes is caused by the presence of a bar and spiral arms and not by geometrical projection effects. Since the inclination of the large scale disk is only  $\simeq 20^\circ$ , one expects almost circular isophotes, and it is reasonable to obtain the light profiles from azimuthal averages instead of canonical ellipse fitting.

In Figure 9 we plot the azimuthally averaged light profiles extracted from the WFPC2 and NICS images. The light profiles have all been rescaled to match the external one of the F814W image. The profiles all match well beyond  $r > 10''$  and the colors of that region can be estimated as  $B - I \sim 1.7$ ,  $R - I \sim 0.4$  and  $I - K \sim 2.1$ . These colors are consistent with other spiral galaxies: for instance de Jong (1996) has shown that the spirals of this Hubble type on average have integrated colors  $B - I = 1.8 \pm 0.2$  (observed 1.7) and

$$B - K = 3.5 \pm 0.3 \text{ (3.8)}.$$

The red feature observed in the color maps around the nucleus results in a flattening of the light profiles which increases at decreasing wavelength. From the figure one can immediately estimate the color excess or reddening for each pair of bands with respect to the external points. Roughly  $E(B - I) \sim 0.8$ ,  $E(R - I) \sim 0.4$  and  $E(I - K) \sim 0.5$ . Assuming the galactic extinction law by Cardelli, Clayton, & Mathis (1989) one finds that with  $A_V \sim 1.2$  mag one can approximately match the observed color excesses ( $A_V \sim 1.2$  implies  $E(B - I) \sim 1.03$ ,  $E(R - I) \sim 0.32$  and  $E(I - K) \sim 0.44$ ). Thus the red feature observed in the color maps is likely to be due to extinction by dust with average value of  $A_V \sim 1.2$  mag.

## 4. Model fitting

### 4.1. The stellar luminosity density

In order to estimate the stellar contribution to the gravitational potential in the nuclear region, we have to derive the stellar luminosity density from the observed surface brightness distribution. This inversion is not unique if the gravitational potential does not have a spherical symmetry. Here, we assume that the gravitational potential is an oblate spheroid (e.g., van der Marel & van den Bosch 1998). We further assume that the principal plane of the potential has the same inclination as the large scale disk ( $i \simeq 20^\circ$ , LEDA and de Vaucouleurs et al. 1991). The knowledge of  $i$ , combined with the observed axial ratio of the isophotes, should directly provide the axial ratio of an axisymmetric light distribution, but the presence of a bar-like structure invalidates this approach since the flattening of the isophotes cannot be ascribed to simple projection effects. Therefore we consider two extreme cases: a spherical and a disk light distribution. The model light profiles are computed taking into account the finite spatial resolution and pixel size of the detector. A detailed description of the relevant formulas for the inversion and fitting procedure is presented in Appendix A.

The light profiles derived from HST images have better spatial resolution than the one derived from ground-based NICS image. However, as shown above, the optical HST images suffer from  $A_V \sim 1.2$  mag extinction in the nuclear region. It

TABLE 1  
BEST FIT PARAMETERS OF THE STELLAR LIGHT DENSITY.

$q$	$\rho_b^{\star \text{ a}}$	$r_b^{\star \text{ b}}$	$\beta^{\star}$	$\rho_b^{\text{ a}}$	$m_b^{\text{ b}}$	$\alpha$	$\beta$	$\chi_{\text{red}}^2$
I band (WFPC2/F814W)								
1.0	1023	0.27	4.2	0.73	12.6	0.9	1.6	10.8
0.1	951	0.31	5.0	5.8	12.6	0.9	1.6	10.5
K band (NICS)								
1.0	910	0.27 <sup>c</sup>	4.2 <sup>c</sup>	0.44	28.0	1.4	3.0	9.8
0.1	609	0.31 <sup>c</sup>	5.0 <sup>c</sup>	1.60	45.9	1.4	6.6	7.7

<sup>a</sup>In units of  $M_{\odot} \text{ pc}^{-3}$  assuming  $\Upsilon = 1$ .

<sup>b</sup>In units of arcsec.

<sup>c</sup>Kept fixed at the value from the previous fit.

is also well known that K band light is a better tracer of mass. Therefore it is useful to use both the HST and ground based light profiles in order to infer the mass profiles. The star cluster is probably washed out by the lower spatial resolution in the NICS image, thus, in order to account for its presence one can determine its geometrical parameters from the fit of the HST light profiles and use them in the fitting the NICS image.

In principle, the WFPC2 images could be reddening corrected by using the color maps in Figure 7 to derive the  $E(B - V)$  map. In order to do this, one might assume that the colors in the nuclear region are constant and equal to those beyond  $10''$  (see Figure 9). For a more detailed description of this procedure see for instance Marconi et al. 2000. However the cluster would be forced to have the same intrinsic color as the galactic disk, which is probably not realistic. Moreover its shape would be affected by PSF differences among the images. Finally it is not clear if the color differences are due entirely to reddening. We therefore decided not to apply any reddening correction and the consequences of this will be discussed in §5.

We first consider the light profile derived from WFPC2/F814W because it is the least sensitive to reddening among the HST images. We then fit

a model light distribution composed of the central star cluster and the more extended component. We assume that the star cluster luminosity density is spherically symmetric with a density law:

$$\rho^{\star}(r) = \rho_b^{\star} \left( 1 + \left( \frac{r}{r_b^{\star}} \right)^2 \right)^{-\beta^{\star}} \quad (1)$$

The extended component has a functional form of the type

$$\rho(m) = \rho_b \left( \frac{m}{m_b} \right)^{-\alpha} \left( 1 + \left( \frac{m}{m_b} \right)^2 \right)^{-\beta} \quad (2)$$

where  $m^2 = x^2 + y^2 + z^2/q^2$  corresponds to the radius in the spherical case and  $q$  is the axial ratio of the mass distribution. This functional form of the extended component is a reasonable description of the central part of the galaxy where the bulge dominates. It is sufficient for our purposes because we are interested in modeling only the inner  $r < 5''$ .

In Equation 2,  $q = 1$  for a spherical light distribution, and  $q = 0.1$  for a disk-like one. These are the two extreme cases. The best fit parameters for the HST light profile are shown in the upper part of Table 1. The left panel in Figure 10

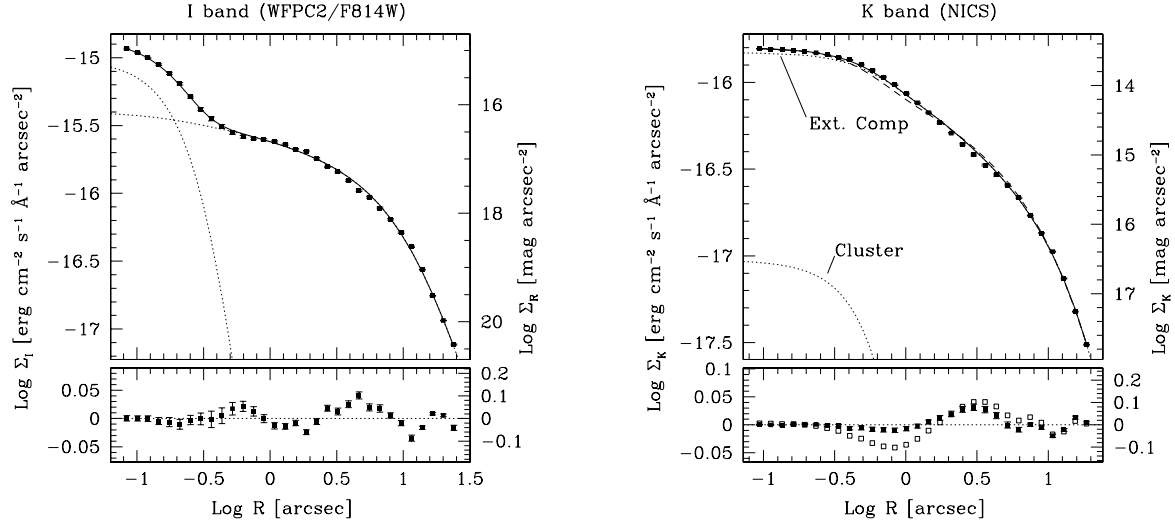


Fig. 10.— Left: fit of the light profile obtained from the WFPC2/F814W data. Right: fit of the NICS/K light profile with the central star cluster and the extended component (the geometrical parameters of the star cluster were determined in the previous fit). In both cases the lower panel shows the fit residuals. The dashed line in the right panel shows the K band fit obtained by fixing the cluster normalization to a value which is 0.6 dex larger than the best fit value. The empty squares show the corresponding residuals.

shows the fit in the spherical case which is visually indistinguishable from the disk case.

Using the geometrical parameters of the cluster determined from the fit to the HST data ( $r_b^*$  and  $\beta^*$ ) we fit the NICS profile, both the spherical and disk case. The results are shown in Table 1. The right panels in Figure 10 show the fit in the spherical case which, as before, is visually indistinguishable from the disk-like case.

The values of the reduced  $\chi^2$  reported in Table 1 are much larger than the expected value of 1 and the main reason can be found in the systematic deviation of the residual around  $3''$  (Figure 10) where the data are systematically lower than the model. This systematic deviation, whose maximum value is  $\sim 0.03$  dex, i.e. 7%, is present in both the optical and near-IR light profile and is caused by the presence of the bar-like feature.

The fits to the light profiles allow an estimate of the I and K magnitudes of the star cluster. With the assumed distance, the cluster luminosity is  $10^{7.3} L_{\odot wI}$  where  $wI$  refers to the F814W band (in this band the Sun has  $M_{\odot wI} = 4.16$ ). In the K band, the cluster has  $10^{7.2} L_{\odot K}$  for the spherical and  $10^{7.1} L_{\odot K}$  for the disk cases ( $M_{\odot K} = 3.286$ ).

These results suggest that the cluster could be blue, with estimated color  $I - K \simeq 0.9$  (or 0.5 in the disk case). The estimate of the K mag of the cluster is however uncertain due to the fact that the cluster is unresolved in the ground based observations. In order to set a limit to the amount of the cluster contribution to the K band light profile, in Figure 10 we also plot the results of the fit when the cluster normalization has been fixed to a value 0.6 dex larger (i.e. the cluster is 1.5 magnitudes brighter) than the best fit value (dashed line). The fit is worse, as clearly indicated by the residuals, and we consider this a firm upper limit for the cluster contribution to the K band light profile. This implies that the observed color of the cluster is  $I - K < 2.4$ . If we assume that the cluster is subjected to  $A_V = 1.2$  mag of extinction (§3.2.1), the upper limit changes to  $I - K < 2.0$ .

Figure 11 shows the circular velocities in the principal plane of the potential expected from the density distributions determined from the fit of the NICS and HST data. In order to match the different rotation curves the circular velocities are plotted for  $\Upsilon_K = 0.5$  or  $\Upsilon_I = 2.3$ , the values derived in §4.2 from fitting the rotation curves. It

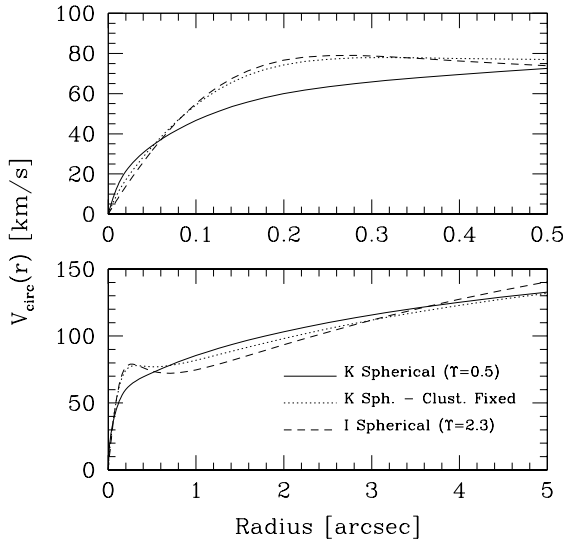


Fig. 11.— Circular velocities in the principal plane of the potential for the density distributions determined from the fit of the NICS and HST data. The circular velocities are derived assuming a spherically symmetric mass distribution and are plotted for  $\Upsilon_K = 0.5$  and  $\Upsilon_I = 2.3$ . The dotted line represent the extreme case in which the cluster normalization in the K band has been fixed to  $+0.6$  dex of the best fit value (see text).

is clear that the rotation curves are very similar beyond  $r > 0.5''$ . However they differ at smaller radii because of the different contribution of the star cluster to the total mass budget. This difference is due to the fact that the mass-to-light ratio has been assumed constant in each band.

#### 4.2. Kinematics

In order to model the gas kinematical data (velocities and widths measured along the slit) we select the simplest possible approach and we assume that the ionized gas is circularly rotating in a thin disk located in the principal plane of the galaxy potential. The latter assumption is not needed if the galaxy potential has a spherical symmetry. We assume that the disk is not pressure supported and we neglect all hydrodynamical effects. Thus the disk motion is completely determined by the gravitational potential which is made of two components: one is stellar and is completely deter-

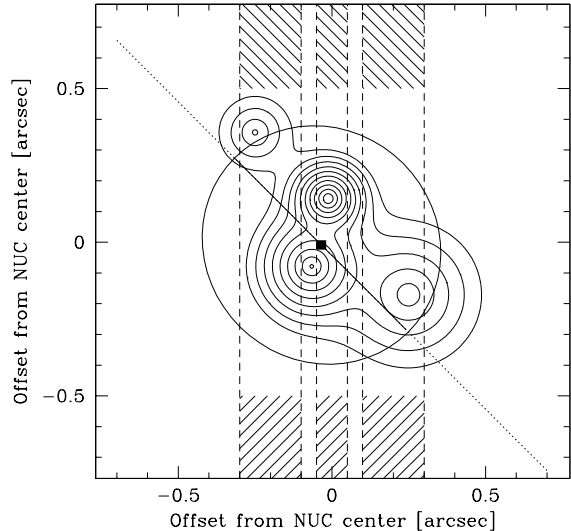


Fig. 12.— Contours of the modelled emission line flux distribution of the nuclear gas disk with over-plotted the slit positions (vertical dashed lines), the position of the kinematic center (filled square), and the line of nodes derived from fitting the kinematic data (solid straight line). The dotted line is the line of nodes of the extended material. The ellipse indicates the nuclear gas disk outer limit for an inclination of  $20^\circ$  with respect to the line of sight.

mined by the mass distribution, derived in the previous section, and by its mass-to-light ratio  $\Upsilon$ . The other one comes from a dark mass concentration (the black hole), spatially unresolved at HST+STIS resolution and defined by its total mass  $M_{\text{BH}}$ . This is the same approach which has been followed in all previous gas kinematical studies of circumnuclear gas disks (e.g. Macchetto et al. 1997; van der Marel & van den Bosch 1998; Barth et al. 2001; Marconi et al. 2001).

In principle, in order to constrain the BH mass, one should compare the emission line profile predicted by the model with the observed one. Even in the simple potential described above, the line profiles can be very complicated, with multiple peaks (Maciejewski & Binney 2001). Nevertheless, as shown in Figure 4, the line profiles are well represented by single gaussians (after subtracting the “blue” component) and therefore we

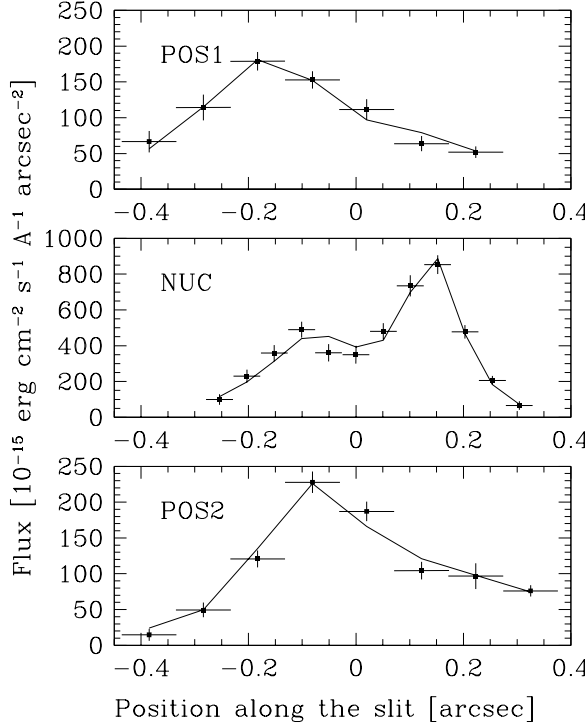


Fig. 13.— The assumed flux distribution compared with the data after folding with the telescope and instrument responses. The model values are connected by straight lines in order to guide the eye.

compare the moments of the line profiles: the average velocity  $\langle v \rangle$  and velocity dispersion  $\sigma$  defined as  $\sigma^2 = \langle v^2 \rangle - \langle v \rangle^2$ . In order to be compared with the observations, the model  $\langle v \rangle$  and  $\sigma$  are computed taking into account the spatial resolution of HST/STIS and the size of the apertures over which the observed quantities are measured. The formulae used to compute velocities, widths and line fluxes and the details of their derivation, numerical computation and model fitting are described in Appendix B. To derive the observed  $\langle v \rangle$  and  $\sigma$ , our approach is to parameterize the observed spectra by fitting them with as many gaussian components as required by the data. Then, components which are not obviously coming from circularly rotating gas can be discarded (e.g. Winge et al. 1998) and the average velocities and line widths can be computed from the remaining ones (this is trivial if, as in the

present case, only a single gaussian component is left). With this approach, the observed and model parameters, are compared. The advantages of our approach are twofold. Firstly, much computational time is saved in computing just  $\langle v \rangle$  and  $\sigma$  instead of the whole line profile. Secondly, modeling the observed emission line profiles in detail requires very high S/N data and it is seldom possible to obtain such high quality data with HST except for a few galaxies (e.g. M87, Macchetto et al. 1997). Even with the high S/N available from 8m class telescopes the matching of the line profiles remains a significant problem (e.g. Cen A, Marconi et al. 2001).

Thus, the model  $\langle v \rangle$  and  $\sigma$  depend on  $\Sigma$ , the intrinsic surface brightness distribution of the emission lines, and on the following parameters:

- $s_o$ , the position of the kinematical center along the slit with respect to the position of the continuum peak;
- $b$ , the distance between the reference slit center of the NUC slit and the kinematical center;
- $i$ , the inclination of the rotating disk;
- $\theta$ , the angle between the disk line of nodes and the slits;
- $V_{\text{sys}}$ , the systemic velocity of the disk;
- $\Upsilon$ , the mass-to-light ratio of the stellar population;
- $M_{\text{BH}}$ , the BH mass.

Not all of these parameters can be independently determined by fitting the observations.

It can be inferred from the equations in Appendix B that  $M_{\text{BH}}$ ,  $\Upsilon$  and  $i$  are directly coupled. This fact has already been discussed in detail by Macchetto et al. (1997) but here we briefly indicate how this coupling can be used to pose a lower limit on the disk inclination  $i$ . Considering the case where no BH is present, the amplitude of the rotation curves depends linearly on  $\Upsilon^{0.5} \sin i$  and its value can be determined by fitting the observations. Therefore  $\Upsilon$  will increase with decreasing  $i$ . An upper limit on  $\Upsilon$  can be certainly set by the largest reasonable value for a very old stellar

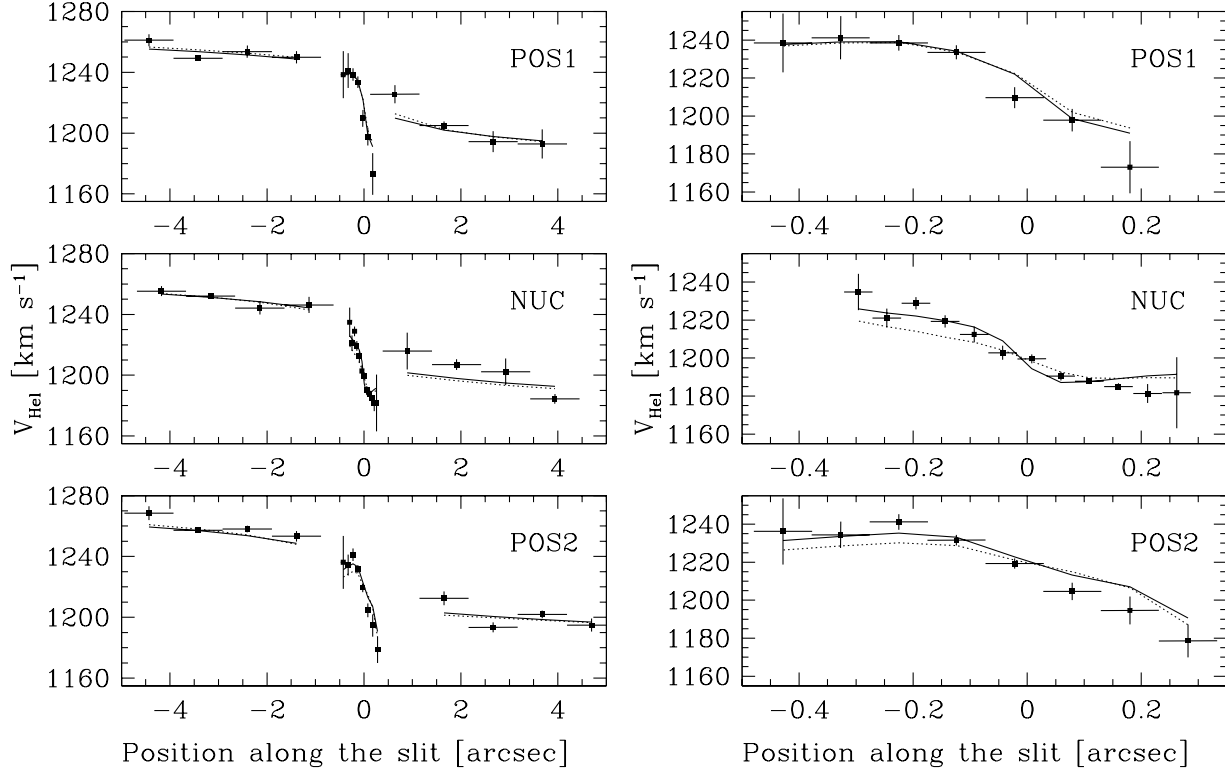


Fig. 14.— Best fit standard model of the observed rotation curves (solid line) compared with the data. The dotted line is the best fit model without a black hole. The model values are connected by straight lines in order to guide the eye. Note that points from external and nuclear regions are not connected because they are kinematically decoupled.

The right panel is a zoom on the nuclear disk region. The plotted model uses the mass density distribution derived from the K band light profile with the assumption of spherical symmetry.

population (e.g. Bruzual & Charlot 1993; Maraston 2000) and this will immediately fix the lower limit for  $i$ . If a BH is present,  $\Upsilon^{0.5} \sin i$  can still be determined from the kinematical data obtained beyond the BH sphere of influence. Of course, the underlying assumption is that both  $\Upsilon$  and  $i$  are constant.

#### 4.2.1. The intrinsic surface brightness distribution of emission lines

The intrinsic surface brightness distribution of emission lines  $\Sigma$  is an important ingredient in the model computations because it is the weight in the averaging of the observed quantities. The ideal situation would be to have an emission line image with spatial resolution higher than the spectra.

Not having that, Barth et al. (2001) have used a deconvolved HST image to model their HST data. This helped them to match the microstructure of the velocity field at large radii, but it is important to remember that the information about the BH mass comes predominantly from within the central unresolved source of unknown luminosity distribution. Our approach is to attempt to match the emission line fluxes as observed in the spectra (or in emission line images) together with a variety of synthetic realizations of this unknown central emissivity distribution. We use this to estimate its impact on the derived value of  $M_{\text{BH}}$ . Thus, we assume simple analytical forms of the line flux distribution which well match the observed one along the slit, after folding with the telescope and



instrument responses as described above.

It is clear from the right panel in Figure 3 that the flux distribution observed at the three slit positions is very complex and cannot be described by a single radially symmetric component in the disk plane. Therefore we choose the approach of modeling directly the flux distribution on the plane of the sky by exploring various simple analytical forms of the line flux distribution. We take the intrinsic light distribution at point  $x, y$  in the plane of the sky in the NUC slit reference frame ( $x$  is the position across the NUC slit while  $y$  is the position along it) to be defined as

$$I(x, y) = \sum_i I_{oi} f_i \left( \frac{r_i}{r_{oi}} \right) \quad (3)$$

where  $f_i$  is a circularly symmetric function of characteristic radius  $r_{oi}$  and weighting factor  $I_{oi}$ . Each component function  $f_i$  is centered at  $(x_{oi}, y_{oi})$ , and  $r_i$  is the radial distance from this location  $r_i = [(x - x_{oi})^2 + (y - y_{oi})^2]^{0.5}$ . This is an approach similar to that of Barth et al. (2001) except that we use a synthetic realization of the line flux map. Although each bright patch is assumed to be circularly symmetric, its material is in circular rotation about the galactic nucleus. Hence patches are constantly shearing rather than moving as coherent units.

The free parameters characterizing the flux distribution are therefore  $(x_{oi}, y_{oi})$ ,  $I_{oi}$  and  $r_{oi}$  and are chosen in order to match the observed flux distribution along the slit after folding the model with telescope and instrument. For example, one of the functional forms used is the combination of 4 exponentials and a constant baseline i.e.  $f_i(r_i/r_{oi}) = \exp(r_i/r_{oi})$ . Figure 12 shows the contours of this line flux distribution which matches the observed profile along the slit after convolving with the instrumental response (see Figure 13).

#### 4.2.2. The standard approach

The standard approach followed so far in gas kinematical analysis is to assume that (i) gas disks around black holes are not warped i.e. they have the same line of nodes and inclinations as the more extended components, and (ii) the stellar population has a constant mass-to-light ratio with radius (e.g. van der Marel & van den Bosch 1998; Barth et al. 2001). In the present case, the blueshift of

the inner disk (§3.1.2) indicates that the standard approach must be generalized to allow for the kinematical decoupling between inner and large scale disks.

We use the emission line flux distribution derived in the previous section and we fix the inclination to  $i=20^\circ$ , i.e. the inclination of the galactic disk. The free parameters of the fit are then  $M_{\text{BH}}$ ,  $\Upsilon$ ,  $s_o$ ,  $b$ ,  $\theta$ ,  $V_{\text{sys}}$  and  $\Delta V_{\text{sys}}$ , the velocity shift of the extended component with respect to the nuclear one. We perform the fit using the mass density profiles derived for the I and K band, both in the spherical and disk cases. The results of the fit are shown in Table 2. Statistical errors at the  $2\sigma$  level on  $\log M_{\text{BH}}$  and  $\log \Upsilon$  are  $\pm 0.2$  and  $\pm 0.1$ , respectively, thus the derived BH mass is  $M_{\text{BH}} = 1^{+0.6}_{-0.7} \times 10^7 M_\odot$ . Figure 14 shows the best fit model (solid line) obtained with the mass density distribution derived from the K band light profile with the assumption of spherical symmetry. The dotted line is the best fit model without a black hole. The left panel of Figure 16 shows the fit of the NUC data from the model with the mass distribution derived from the I band. Figures 14 and 16, indicate that a model with no BH cannot account for the observed nuclear rotation curve, producing a velocity gradient which is shallower than observed. Note that the position angle of the line of nodes, a free parameter of the fit, is the same as the one inferred from the large scale CO velocity map by Sakamoto et al. (1999). This supports the assumption that the nuclear disk is the continuation at small scales of the galactic disk. However the fit confirms that the nuclear disk is blueshifted by  $\sim 10 \text{ km s}^{-1}$  with respect to the extended component and this argues against the assumption in previous sentence. The fit is greatly improved if a velocity shift of  $8 \text{ km s}^{-1}$  is allowed for the POS2 data. This velocity shift is the consequence of an error on the absolute wavelength calibration of the POS2 data and is well within the expected STIS performances (Leitherer et al. 2001).

The value of  $\Upsilon$  in the K band derived from the fit varies between 0.2 (disk light distribution) and 0.5 (spherical light distribution). This range of values is in good agreement with the typical K-band mass-to-light ratios of spiral bulges (Moriando, Giovanardi & Hunt 1998). Similarly the value of  $\Upsilon$  in the I band ranges between 2.2 and

TABLE 2  
MODEL FIT RESULTS IN THE STANDARD APPROACH.

Band (a)	$q$ (b)	$\log M_{\text{BH}}$ (c)	$\Upsilon$ (d)	$s_o$ (e)	$b$ (e)	$\theta$ (f)	$V_{\text{sys}}$ (g)	$\Delta V_{\text{sys}}$ (g)	$\chi^2_{\text{red}}$ (h)
K	1.0	7.04	0.52	-0.04	0.02	-45	1212	11	2.32
K	1.0	0.0*	1.00	-0.09	0.06	-58	1211	11	2.88
K	0.1	7.09	0.22	-0.07	0.08	-32	1213	11	2.13
I	1.0	6.86	2.28	-0.01	0.00	-42	1210	12	1.86
I	1.0	0.0*	2.65	-0.03	0.03	-45	1210	12	2.09
I	0.1	7.14	1.65	-0.03	0.01	-47	1212	10	2.22

<sup>a</sup> Band from which the mass density profile was derived.

<sup>b</sup> Assumed axial ratio of the mass distribution.

<sup>c</sup> Log of BH mass in units of  $M_{\odot}$ .

<sup>d</sup> Mass-to-light ratio in used band.

<sup>e</sup> Arcsec

<sup>f</sup> Degrees

<sup>g</sup>  $\text{km s}^{-1}$

<sup>h</sup> Reduced  $\chi^2$ .

\* The parameter was fixed to this value.

TABLE 3  
MODEL FIT RESULTS IN THE ALTERNATIVE APPROACH.

Band	$q$	$\log M_{\text{BH}}$	$\Upsilon$	$s_{\circ}$	$b$	$\theta$	$i$	$V_{\text{sys}}$	$\chi^2_{\text{red}}$
(a)	(b)	(c)	(d)	(e)	(e)	(f)	(f)	(g)	(h)
Extended Component									
K	1.0	0.0*	0.48	0.0*	0.0*	$-43^{\circ}$	$20^{\circ}$	1224	2.7
K	0.1	0.0*	0.31	0.0*	0.0*	$-43^{\circ}$	$20^{\circ}$	1224	2.7
I	1.0	0.0*	2.29	0.0*	0.0*	$-43^{\circ}$	$20^{\circ}$	1224	2.5
I	0.1	0.0*	1.38	0.0*	0.0*	$-43^{\circ}$	$20^{\circ}$	1224	2.5
Nuclear Disk									
K	1.0	$<6.8$	1.29	0.0	$-0.05$	$-40^{\circ}$	$20^{\circ}$	1204	0.66
K	1.0	$<6.6$	$0.48^{\star}$	$-0.01$	$-0.04$	$-39^{\circ}$	$35^{\circ}$	1205	0.67
K	0.1	$<6.8$	0.88	$-0.01$	$-0.05$	$-40^{\circ}$	$20^{\circ}$	1205	0.69
I	1.0	$<6.8$	4.05	$-0.01$	$-0.04$	$-41^{\circ}$	$20^{\circ}$	1206	0.60
I	0.1	$<6.8$	3.77	0.00	$-0.04$	$-41^{\circ}$	$20^{\circ}$	1205	0.58

<sup>a</sup> Band from which the mass density profile was derived.

<sup>b</sup> Assumed axial ratio of the mass distribution.

<sup>c</sup> Log of BH mass in units of  $M_{\odot}$ .

<sup>d</sup> Mass-to-light ratio in used band.

<sup>e</sup> Arcsec

<sup>f</sup> Degrees

<sup>g</sup>  $\text{km s}^{-1}$

<sup>h</sup> Reduced  $\chi^2$ .

<sup>\*</sup> The parameter was fixed to this value.

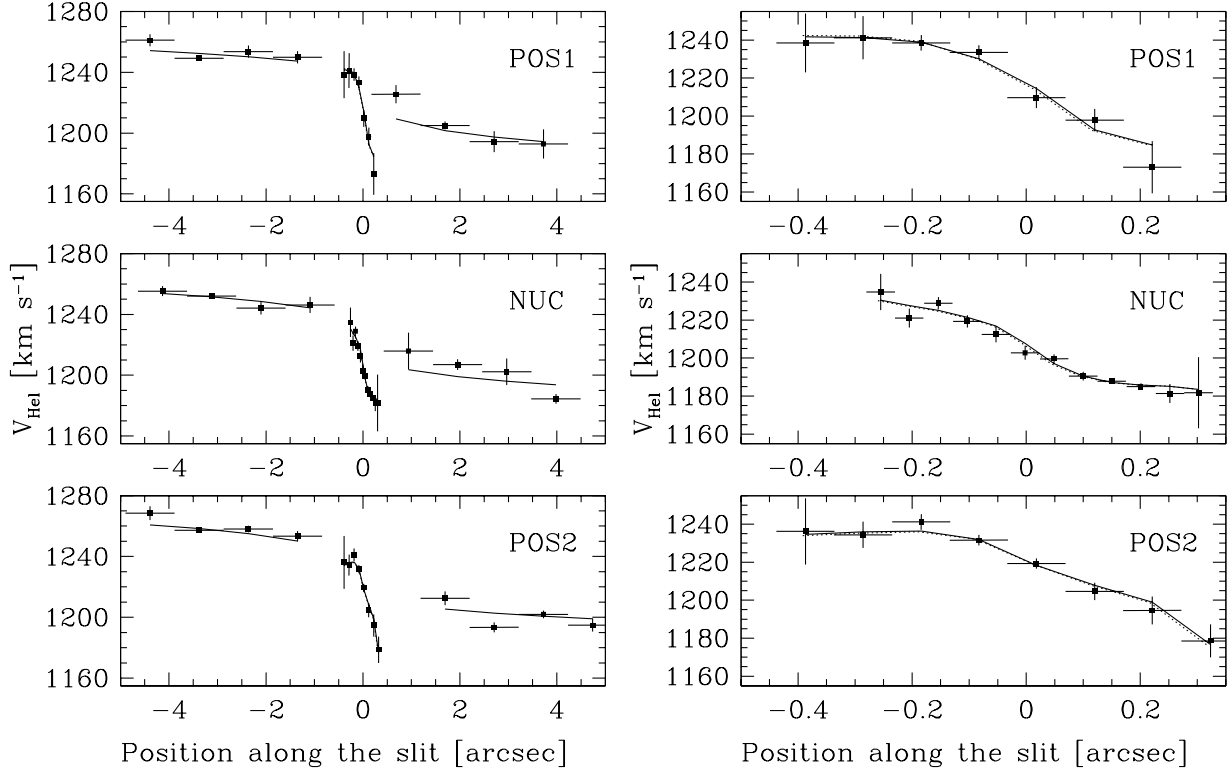


Fig. 15.— Best fit alternative model of the observed rotation curves compared with the data. The solid line is the best fit model obtained by fixing  $i$  and varying  $\Upsilon$  while the dotted line represent the case in which  $i$  has been varied and  $\Upsilon$  kept fixed. The model values are connected by straight lines in order to guide the eye. Note that points from external and nuclear regions are not connected because they are kinematically decoupled. The right panel is a zoom on the nuclear disk region. The plotted model uses the mass density distribution derived from the K band light profile with the assumption of spherical symmetry.

3.6 in agreement with measurements within the inner 2 kpc of spiral galaxies (Giovanelli & Haynes 2002).

#### 4.2.3. Alternative model: the decoupled nuclear disk

To date, everyone who has determined a central BH mass from gas kinematics assumed that the disks are unwarped, i.e. coplanar at all radii, and that the stellar mass-to-light ratio is constant with radius.

The high surface brightness and velocity offset of the nuclear disk with respect to the extended component presented in §3 indicate that, at least for NGC 4041, this assumption could be untrue. The nuclear and large scale disks might be char-

acterized by different geometrical properties like position angle of the line of nodes, inclination and systemic velocity. Recently Cappellari et al. (2002) have shown a discrepancy between the BH mass in IC 1459 determined from gas kinematical (Verdoes Klein et al. 2000) and stellar dynamical models. The authors propose that a possible solution to this discrepancy could be an error on the assumed gas disk inclination.

Therefore, in the alternative approach presented here, we first fit the extended component data in order to determine the mass-to-light ratio  $\Upsilon$  of the stellar component to be used in the fit of the nuclear data. For the extended component we assume a constant line flux distribution and determine  $\Upsilon$  in the two extreme cases of the spherical

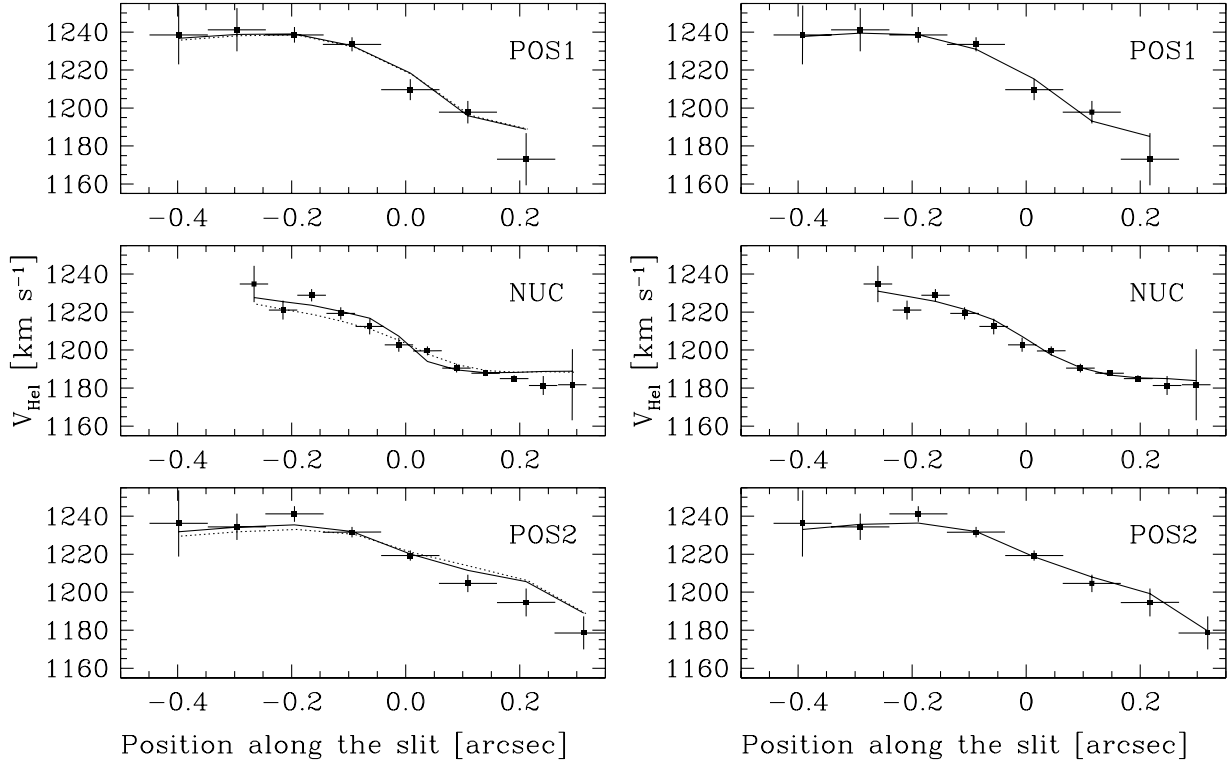


Fig. 16.— Best fit models of the observed rotation curves computed using the mass densities derived from the I band light profiles. The model values are connected by straight lines in order to guide the eye. The left panel refers to the standard model (the dotted line is the model without a BH) while the right panel refers to the alternative model.

and disk-like light distribution (i.e. with an axial ratio of  $q = 0.1$ ).

From the CO velocity map by Sakamoto et al. (1999) the PA of the kinematic line-of-nodes is  $\text{PA} = 86^\circ$ , i.e. almost exactly East–West. Since the PA of the slit in the STIS observations is  $43^\circ$ , this means that the angle between the slit and the disk line of nodes is  $\theta = -43^\circ$  (for the definition of  $\theta$  see Appendix B). We also assume that the inclination of the disk is  $i = 20^\circ$ , as specified in the previous section. The CO velocity map also clearly indicates that the large scale velocity field is circularly symmetric.

The fitted circular rotation curves of the extended gas are shown in Figure 15. The derived  $\Upsilon$  for the spherical or disk geometry are shown in Table 3 for the mass density profiles derived from both the K and I band light. In our derivation

we allowed for a constant velocity shift between the data points in the off-nuclear slit positions and the nuclear one. This is caused by the uncertainty in the absolute wavelength calibration, and is very small,  $-1 \text{ km s}^{-1}$  and  $8 \text{ km s}^{-1}$  for POS1 and POS2 respectively.

Similarly to the results of the standard model, mass-to-light ratios in the K and I band are consistent with typical values for the central regions of spiral galaxies.

We now fit the nuclear data ( $r \leq 0''.4$ ) allowing for values of  $\Upsilon$  or  $i$  different from those of the extended component. Results of the fit are shown in Figure 15 and in Table 3. The right panel of Figure 16 shows the fit of the NUC data from the model with the mass distribution derived from the I band.

In all these cases the BH mass has been set to

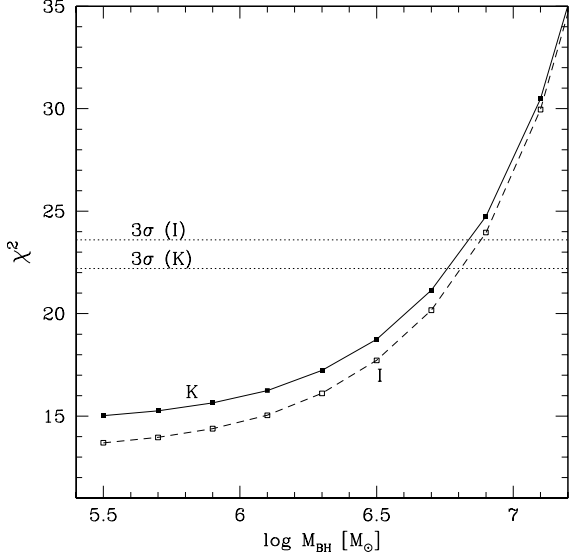


Fig. 17.— Statistical upper limits on the BH mass in the alternative approach for the cases in which the mass density has been derived by the I and K band light profiles.

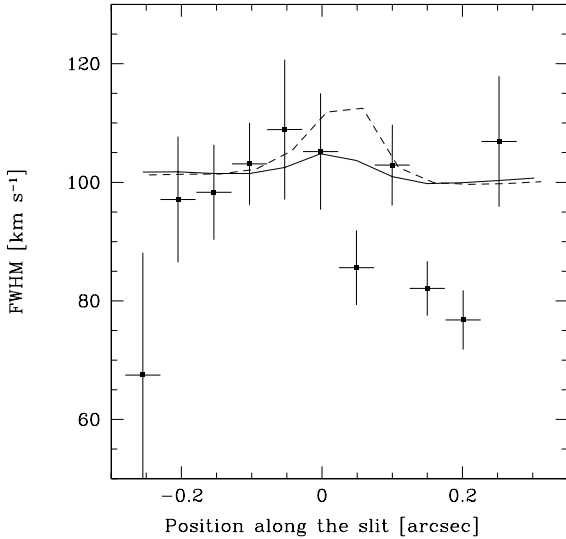


Fig. 18.— Observed and model FWHMs at the NUC position. The solid line is the case without a BH (alternative model) and the dashed line is with a  $10^7 M_{\odot}$  BH (standard model). The assumed intrinsic velocity dispersion is  $35 \text{ km s}^{-1}$ .

zero and the goodness of the fit suggest that no BH is needed to fit the data with this approach. We estimate the upper limit on the BH mass by a 1 parameter variation, i.e. we assign a fixed value of  $M_{\text{BH}}$  and we perform the fit. When we have  $\Delta\chi^2 \geq 1, 4, 9$  we have reached the 1,2,3  $\sigma$  upper limit. As an example, in Figure 17, we show the  $\chi^2$  plot corresponding to the K and I band spherical cases. There the  $3\sigma$  upper limit is  $10^{6.8} M_{\odot}$ .

From Table 3 it can be seen that the position of the nucleus along and across the slit is independent of the assumed mass distribution. The inclination varies, but like  $\Upsilon$ , is just a scaling factor. Indeed varying  $\Upsilon$  produces the same results, as shown in the same table. The angle between the slit and the line of nodes is very well determined in the range  $-39 - -41^\circ$ . This means that the PA of the kinematical line of nodes is  $43^\circ$  (the PA of the slit) minus  $-40^\circ$  i.e.  $\sim 83^\circ$  consistent with the PA of the kinematical line of nodes on large scales. The systemic velocity is  $1204 - 1206 \text{ km s}^{-1}$  and is definitely blueshifted with respect to the extended rotation where it is  $1224 \text{ km s}^{-1}$ .

As pointed out by Barth et al. (2001) the FWHM of the lines might be a worrisome issue in the sense that FWHM much larger than instrumental might indicate motions which could deviate from circular (apart from the broadening of the line due to unresolved rotation around a point mass). In Figure 18 we plot the observed FWHMs and compare them with the expected one in the framework of the alternative model assuming an intrinsic velocity dispersion of only  $35 \text{ km s}^{-1}$ . Also the dashed line represents the case with a  $10^7 M_{\odot}$  BH showing that, in this case, the FWHM cannot pose good constraints on the BH mass.

## 5. Discussion

### 5.1. How the BH mass determination is affected by assumptions.

In §4.2 we have shown that the inclination of the nuclear disk,  $i$ , and the mass-to-light ratio of the stellar population,  $\Upsilon$ , play a critical role in detecting the presence of a nuclear BH. The *standard* model, in which  $i$  and  $\Upsilon$  are the same for the nuclear disk and the more extended galactic disk, requires the presence of a BH with  $M_{\text{BH}} = 1_{-0.7}^{+0.6} \times 10^7 M_{\odot}$  (§4.2.2). Conversely, al-

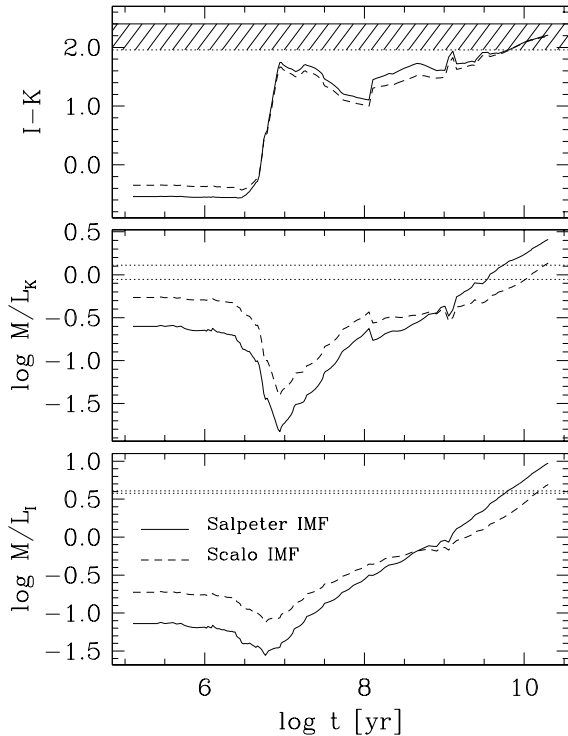


Fig. 19.— From top to bottom:  $I - K$ ,  $\log M/L_K$  and  $\log M/L_I$  vs time for a single stellar population (instantaneous burst) with solar metallicity (models by Bruzual & Charlot 1993, updated in 1996). The solid and dashed line are for a Salpeter (1955) and a Scalo (1986) IMF respectively. In the upper panel, the solid horizontal line represents the observed upper limit on the  $I - K$  color. The dotted line is the same upper limit after correction for  $A_V = 1.2$  mag. In the central and lower panel, the horizontal dotted lines indicates the range of mass-to-light ratios allowed by the observations.

lowing either  $\Upsilon$  or  $i$  to vary, the kinematical data can be fit without a BH (the so-called *alternative* model, §4.2.3) and  $M_{\text{BH}} < 6 \times 10^6 M_\odot$ . These results show a caveat in gas kinematical searches, where it is always assumed that  $i$  and  $\Upsilon$  are constant at all radii.

To distinguish between the standard and alternative models it is necessary to find some extra physical constraints. In particular the value of mass-to-light ratio  $\Upsilon$  determined from the observations should be consistent with realistic stellar

populations (see §4.2). Little can be said about  $i$  which in contrast with the other geometrical parameter of the disk,  $\theta$ , is poorly constrained by the rotation curves. Usually one can infer an estimate of  $i$  from the morphology of the disk observed in emission line images, especially in E and S0 galaxies (e.g. van der Marel & van den Bosch 1998; Barth et al. 2001). The root of the problem lies in the coupling between  $M_{\text{BH}}$ ,  $\Upsilon$  and  $i$  that arises because they are all essentially scaling factors on the amplitude of the rotation curves.

In the *standard* approach (Table 2)  $M_{\text{BH}}$  does not depend on the assumed mass density profile (either from the K or I band). The angle  $\theta$ , which is a free parameter of the fit, is quite well constrained around  $-40^\circ$ , i.e. the PA of the kinematical line of nodes is the same as the one at large scales derived from the 2D CO map by Sakamoto et al. (1999). The constancy of  $\theta$ , which is not an intrinsic parameter of the system but only depends on the galaxy orientation in the plane of the sky, suggests that  $i$  ( $\Delta i$  between the nuclear and galactic disk is an intrinsic parameter of the system) should also be constant. No similar argument can be placed on  $\Upsilon$  which can then be allowed to vary and it is then possible to fit the kinematical data without the presence of a BH. This requires that  $\Upsilon$  in the nuclear region is a factor of  $\sim 2$  larger than that in the extended disk.

To verify if this  $\Upsilon$  is consistent with the observed colors, we plot in Figure 19  $I - K$ ,  $\Upsilon_K$  and  $\Upsilon_I$  as a function of time from the burst for a single stellar population experiencing an instantaneous burst of star formation. We have used the models by Bruzual & Charlot (1993), updated in 1996, we considered solar metallicities, Salpeter (1955) and Scalo (1986) IMF (solid and dashed lines in the figure), and used the theoretical stellar libraries. The solid line in the upper panel marks the upper limit we placed on the  $I - K$  color of the stellar cluster (§4.1); the dotted line marks the same upper limit but dereddened for  $A_V = 1.2$  mag (§3.2.1). Finally, the dotted lines in the central and lower panels shows the  $\Upsilon$  required to fit the data in the alternative model both for the spherical and disk-like distribution of stars. The  $\Upsilon$ s implied by the analysis are thus consistent with a very old nuclear star cluster, with age  $\sim 10$  Gyr. This is apparently in contrast with the high H $\alpha$  equivalent width measured in the nuclear spectrum,  $\simeq 70 \text{ \AA}$ ,

which seems to require the presence of very young stars. A possibility is that the  $H\alpha$  emission is not due to young stars but to a low luminosity AGN and, indeed, the total  $H\alpha$  luminosity in the nuclear region is  $L(H\alpha) = 4.9 \times 10^4 L_\odot$  corresponding to the low end of the  $L(H\alpha)$  distribution for AGNs (Ho, Filippenko, & Sargent 1997). To prove that the emission lines are excited by an AGN, one could use the so-called diagnostic line ratios  $[NII]/H\alpha$  and  $[OIII]/H\beta$  (e.g. Osterbrock 1989). Ground based spectra with  $1''$  resolution (Axon et al. in preparation) indicate that this object is on the boundary between HII regions and LINERs with  $[NII]/H\alpha \sim 1$  and  $[OIII]/H\beta < 0.5$ . Unfortunately the spectra coverage of our HST data is limited to 6500-7000 Å region but the the  $[NII]/H\alpha$  ratio at  $0''.1$  resolution remains similar to that observed from the ground suggesting that the same could be true for the  $[OIII]/H\beta$ .

If on the other hand the star cluster is young, it can fully account for the  $H\alpha$  emission. Assuming case B recombination, the  $L(H\alpha)$  luminosity implies an ionizing photon rate of  $Q(H) \sim 2 \times 10^{50} s^{-1}$  (e.g. Osterbrock 1989), which corresponds to  $\sim 2 - 20$  O stars (Panagia 1973). When confronted with stellar population synthesis model (Leitherer et al. 1999) the observed  $H\alpha$  equivalent width indicates an age of  $\sim 10^7$  yr. In this case, as shown in Figure 19, the I band mass-to-light ratio is more than a factor ten lower and the fit of the kinematical data requires a BH even in the alternative model. However when using the stellar mass density profile derived from the K band, the data can still be explained by stars alone. The reason is that the contribution of the star cluster to the total light density profile is small, as can be seen from the rotation curves in Figure 11. Note that in order to explain the high  $[NII]/H\alpha$  ratio with photoionization from stars one needs to allow for higher-than-solar N abundances in the nucleus as has been suggested many times in the past since the work by Burbidge & Burbidge (1962).

In order to proceed further and firmly establish the age of the star cluster, one needs HST/NICMOS infrared images of the nuclear region. The optical to near-IR colors of the star cluster constrain its age and mass-to-light ratio. Moreover with HST/STIS blue spectra one can measure the  $[OIII]/H\beta$  ratio, in order to estimate the AGN contribution, and verify the existence of

deep H Balmer lines in absorption expected if the cluster is young.

The other assumptions behind the modeling are the shape of the stellar density profile (spherical vs disk-like, I vs K band, effects of reddening), the intrinsic flux distribution of the emission lines and, finally, the assumption of circular motions.

The stellar density profile depends on  $q$ , the intrinsic axis ratio of the extended mass distribution, and on the relative importance between the nuclear star cluster and the extended stellar component. As shown in the previous section, the four cases examined there cover the most extreme cases: spherical or disk-like distribution of the extended component ( $q = 1$  and  $q = 0.1$  respectively), stellar cluster which gives a small contribution to the total stellar density distribution (K band) or which dominates over the nuclear disk size i.e.  $r < 0''.4$  (I band). From Tables 2 and 3 we can conclude that the value of the BH mass or its upper limit do not depend on the assumed stellar density profile. From the same table it can be seen that the position of the nucleus along and across the slit is also independent of the assumed mass distribution. In §4.1 we decided not to apply a reddening correction to the light profiles because of the uncertainties involved. This reddening correction would have affected the values of the mass-to-light ratios derived from the rotation curves (see §4.2) whose accurate measurement is not the aim of this paper. Roughly, assuming an average  $A_V = 1.2$  mag (§3.2.1), the I light would increase by  $\sim 70\%$  and  $\Upsilon_I$  would decrease by the same amount (-0.2 in log). The K light would similarly increase only by  $\sim 10\%$  with a similar decrease in  $\Upsilon_K$  (-0.04 in log). These corrections would have a marginal effect for the conclusions on the cluster age derived in Figure 19. Finally the reddening correction effects on the shape of the stellar light/mass density profiles, would be negligible for the estimate of the BH mass upper limit. Indeed, the same value is obtained regardless of the use of mass density profiles derived from the I or K band light which are very differently affected by reddening.

Another important issue is the influence of the intrinsic line flux distribution on  $M_{BH}$ . We have tried several other different realizations of the observed flux distribution by varying both the number of components and the functional form of



single components (exponential, gaussian, power law). We have found that accurately describing the observed flux distribution is important. Models that did not do this produced fits significantly worse than those described in the previous section. When the fits of fluxes and velocities are acceptable,  $M_{\text{BH}}$  or its upper limit do not depend on the assumed flux distribution.

The assumption of circular motions is probably one of the most critical ones. Circular motions in gaseous disks are expected due to the dissipative nature of the gas, however anisotropies in the stellar potential rapidly lead to non-circular streaming (e.g., Athanassoula 1992). The effect of non-circular motions would be that of “distorting” the rotation curves and increasing the intrinsic line width of the gas. Therefore, obtaining very good fits ( $\chi^2_{\text{red}} < 1$ ) of the rotation curves in the alternative model strengthens our confidence on the assumption of circular motions. This assumption is also supported by the small intrinsic line width ( $\sigma \simeq 35 \text{ km s}^{-1}$ ) required by the observations. Indeed  $\sigma/v_{\text{circ}}$  can be used to quantify the effects of turbulence or non-circular motions on the BH mass determination (e.g. Verdoes Klein et al. 2000; Barth et al. 2001). For the best fitting models  $\sigma/v_{\text{circ}}$  is always less than 0.4 (provided that there is a BH with a mass close to the upper limit in the case of the alternative models). This is similar to what Barth et al. (2001) found in the case of their best fit model of NGC 3245. There the effect of the asymmetric drift correction, a possible way to include non-circular motions in the analysis (e.g. Binney & Tremaine 1987), is that to increase the estimate of the BH mass by just 10%. Apart from these qualitative arguments, the presence of significant non-circular motions cannot be excluded and it is not possible at the moment to quantify their effects on the method we have adopted and described here.

Non-circular motions are certainly present in the nuclear region of NGC 4041 as indicated by the presence of the blue wing, but these have been singled out in the deblending procedure as in Winge et al. (1998).

## 5.2. The blueshift of the nuclear disk

A proposed explanation for the blueshift observed in the nuclear disk is that the star cluster is oscillating across the galactic plane. In this pic-

ture, the cluster is bound to the galaxy, is old and has a large  $\Upsilon$  ensuring that it is massive enough and not subjected to tidal disruption.

Any velocity component perpendicular to the disk will give a large contribution to the observed velocity because the galaxy is almost face-on. If the cluster is oscillating across the galactic plane, the observed blueshift may be translated into a velocity modulus of similar magnitude. Thus, the cluster velocity ( $\sim 10 - 20 \text{ km s}^{-1}$ ) is smaller than the rotational velocity (see Figure 11) and the cluster is bound to the galaxy. If the cluster is very massive, as in the alternative model, then the gravitational potential over the star cluster size is dominated by the star cluster itself and it is not subjected to tidal disruption. Also in this picture the gaseous disk is completely dominated by the gravitational potential of the star cluster. The total cluster mass within  $r < 0''.3$  as derived from the I-band mass density profile (the one in which the cluster dominates) is  $\sim 6 \times 10^7 M_{\odot}$  and this gives an average density of  $\simeq 200 M_{\odot}/\text{pc}^{-3}$ , not an unusually high value, since it can be found in galactic globular clusters (Pryor & Meylan 2002).

In the picture in which the cluster is young (from the fit of the K band we have  $I - K = 0.9$ , i.e.  $\sim 10^7 \text{ yr}$  from Figure 19), the stability against tidal disruption could pose a problem, since the mass in the nuclear region is completely dominated by the bulge stars. However, this problem could be solved if the lifetime of the cluster against tidal disruption is less than or equal to the cluster age.

## 5.3. $M_{\text{BH}}$ - galaxy correlations

It is now clear that a large fraction of hot spheroids contain a BH and, moreover, it seems that the hole mass is proportional to the mass (or luminosity) of the host spheroid. Quantitatively,  $M_{\text{BH}}/M_{\text{sph}} \approx 0.001$  (e.g. Merritt & Ferrarese 2001). This relation is still controversial, however, both because the sensitivity of published searches is correlated with bulge luminosity, and because there is substantial scatter in  $M_{\text{BH}}$  at fixed  $M_{\text{sph}}$ . Recently Ferrarese & Merritt (2000) and Gebhardt et al. (2000) have shown that a tighter correlation holds between the BH mass and the velocity dispersion of the bulge. The two groups however find two different slopes of the correlation,  $M_{\text{BH}} \propto \sigma_{\star}^5$  and  $M_{\text{BH}} \propto \sigma_{\star}^4$  respectively

(Tremaine et al. 2002). Clearly, any correlation of black hole and spheroid properties would have important implications for theories of galaxy formation in general, and bulge formation in particular. Indeed, several authors have shown that the slope of the  $M_{\text{BH}}-\sigma_*$  correlation yields information on the formation process. If the formation process is self-regulated, i.e. if the BH growth is limited by radiation pressure,  $M_{\text{BH}} \propto \sigma_*^5$  (Silk & Rees 1999). Conversely if the growth is regulated by ambient conditions  $M_{\text{BH}} \propto \sigma_*^4$  (Adams, Graff & Richstone 2000; Cavaliere & Vittorini 2001). The uncertainties on the slope of the  $M_{\text{BH}}-\sigma_*$  correlation do not allow one to distinguish between the two cases. To solve this problem more BH mass measurements are needed in the low mass range ( $10^6$ - $10^7 M_\odot$ ) where spiral galaxies are expected to fit.

These correlations are also very important to estimate BH masses quickly and easily instead from very complex dynamical and kinematic measurements. Therefore the quantities involved in the correlations must be measured as carefully as possible in order to reduce the scatter to its intrinsic value. For instance it has been shown that with careful estimates of the bulge luminosity the  $M_{\text{BH}}-L_{\text{sph}}$  correlation has the same scatter as the  $M_{\text{BH}}-\sigma_*$  correlation, in contrast with previous claims (McLure & Dunlop 2002).

Given the low value of the BH mass in NGC 4041,  $M_{\text{BH}} < 2 \times 10^7 M_\odot$ , it is worthwhile to verify the relation of this galaxy with the proposed correlations. The B magnitude from the RC3 catalogue is 11.9 becoming 11.8 after extinction correction (see NED). The morphological type is Sbc/Sc and  $T = 4.0 \pm 0.3$ . From Simien & de Vaucouleurs (1985) the bulge to total luminosity ratio is  $\simeq 0.16$  resulting in  $\Delta m = 2$ . Thus the bulge magnitude is 13.8. The adopted distance, 19.5 Mpc, corresponds to a distance modulus of 31.5 thus the absolute bulge magnitude is  $-17.7$  corresponding to  $1.8 \times 10^9 L_{B\odot}$ . The best fit of the  $M_{\text{BH}} - L_{B,\text{sph}}$  correlation gives  $M_{\text{BH}} = 0.8 \times 10^8 (L_{B,\text{sph}}/10^{10} L_{B\odot})^{1.08}$  (Kormendy & Gebhardt 2001). Thus the expected BH mass in NGC 4041 would be  $1.2 \times 10^7 M_\odot$ , in agreement with the BH mass estimate or upper limit. The best fit of the  $M_{\text{BH}} - \sigma_*$  correlation gives  $M_{\text{BH}} = 1.3 \times 10^8 (\sigma_*/200 \text{ km s}^{-1})^{4.0}$  (Tremaine et al. 2002) or  $M_{\text{BH}} = 1.4 \times 10^8 (\sigma_*/200 \text{ km s}^{-1})^{4.8}$  (Merritt & Ferrarese 2001). Using INTEGRAL/WYFFOS

at the WHT, we have recently measured the stellar velocity dispersion in the central  $2''$  of NGC 4041 (Batcheldor et al., in preparation). With  $\sigma_* = 95 \pm 5 \text{ km s}^{-1}$ , the expected BH masses are then  $7 \times 10^6 M_\odot$  and  $4 \times 10^6 M_\odot$ , both consistent with the result from this paper.

Since the main goal of our project is to determine whether or not spirals do in fact follow the  $M_{\text{BH}}-L_{\text{sph}}$  and  $M_{\text{BH}}-\sigma_*$  relations, it is important to observe also objects which, a-priori, are expected to have marginally or non detectable BHs. Indeed, even if the present measurement is only an upper limit, this is still useful in ruling out the presence of unusually massive central BHs in late type spiral galaxies.

## 6. Conclusions

We presented HST/STIS spectra of the Sbc spiral galaxy NGC 4041 which were used to map the velocity field of the gas in its nuclear region. We detected the presence of a compact ( $r \simeq 0''.4 \simeq 40 \text{ pc}$ ), high surface brightness, circularly rotating nuclear disk cospatial with a nuclear star cluster. This disk is characterized by a rotation curve with a peak to peak amplitude of  $\sim 40 \text{ km s}^{-1}$  and is systematically blueshifted by  $\sim 10 - 20 \text{ km s}^{-1}$  with respect to the galaxy systemic velocity.

We have analyzed the kinematical data assuming that the stellar mass-to-light ratio is constant with radius and that the gaseous disk is not warped, having the same inclination as the large scale galactic disk. We have found that, in order to reproduce the observed rotation curve, a dark point mass of  $(1_{-0.7}^{+0.6}) \times 10^7 M_\odot$  is needed, very likely a supermassive BH.

However the observed blueshift suggests the possibility that the nuclear disk could be dynamically independent. Following this line of reasoning we have relaxed the standard assumptions varying the stellar mass-to-light and the disk inclination. We have found that the kinematical data can be accounted for by the stellar mass provided that either the mass-to-light ratio is increased by a factor of  $\sim 2$  or the inclination is allowed to vary. This model resulted in a  $3\sigma$  upper limit of  $6 \times 10^6 M_\odot$  on the mass of any nuclear black hole.

Combining the results from the standard and alternative models, the present data only allow us to set an upper limit of  $2 \times 10^7 M_\odot$  to the mass of

the nuclear BH.

If this upper limit is taken in conjunction with an estimated bulge B magnitude of  $-17.7$  and with a central stellar velocity dispersion of  $\simeq 95 \text{ km s}^{-1}$ , the putative black hole in NGC 4041 is not inconsistent with both the  $M_{\text{BH}}-L_{\text{sph}}$  and the  $M_{\text{BH}}-\sigma_*$  correlations.

Support for proposal GO-8228 was provided by NASA through a grant from the Space Telescope Science Institute, which is operated by the Association of Universities for Research in Astronomy, Inc., under NASA contract NAS 5-26555

This work was partially supported by the Italian Space Agency (ASI) under grants I/R/35/00 and I/R/112/01.

This work was partially supported by the Italian Ministry for Instruction, University and Research (MIUR) under grants Cofin00-02-35 and Cofin01-02-02

We thank Peter Erwin for useful discussions and the referee, Aaron Barth, for careful reading of the manuscript, suggestions and comments which improved the paper.

This publication makes use of the LEDA database (<http://leda.univ-lyon1.fr>).

This publication makes use of data products from the Two Micron All Sky Survey, which is a joint project of the University of Massachusetts and the Infrared Processing and Analysis Center/California Institute of Technology, funded by the National Aeronautics and Space Administration and the National Science Foundation.

## REFERENCES

- Adams, F. C., Graff, D. S., & Richstone, D. O. 2001, *ApJ*, 551, L31
- Athanassola, E. 1992, *MNRAS*, 259, 345
- Baffa, C. et al. 2001, *A&A*, 378, 722
- Bahcall, J. N., & Wolf, R. A. 1976, *ApJ*, 209, 214
- Barth, A. J., Sarzi, M., Rix, H., Ho, L. C., Filippenko, A. V., & Sargent, W. L. W. 2001, *ApJ*, 555, 685
- Binney, J., & Mamon, G. A. 1982, *MNRAS*, 200, 361
- Binney, J., & Merrifield, M. 1998, *Galactic Astronomy*, (Princeton, NJ: Princeton University Press)
- Binney, J., & Tremaine, S. 1987, *Galactic Dynamics*, (Princeton, NJ: Princeton University Press)
- Böker, T., Laine, S., van der Marel, R. P., Sarzi, M., Rix, H., Ho, L. C., & Shields, J. C. 2002, *AJ*, 123, 1389
- Bower, G. A., et al. 1998, *ApJ*, 492, L111
- Bowers, C. & Baum, S. 1998, STIS Instrument Science Rep. 98-23 (Baltimore: STScI)
- Braatz, J. A., Wilson, A. S., & Henkel, C. 1997, *ApJS*, 110, 321
- Bruzual, A. G., & Charlot, S. 1993, *ApJ*, 405, 538
- Burbidge, E. M. & Burbidge, G. R. 1962, *ApJ*, 135, 694
- Cappellari, M., Verolme, E. K., van der Marel, R. P., Kleijn, G. A. V., Illingworth, G. D., Franx, M., Carollo, C. M., & de Zeeuw, P. T. 2002, *ApJ*, 578, 787
- Cardelli, J. A., Clayton, G. C., & Mathis, J. S. 1989, *ApJ*, 345, 245
- Carollo, C. M., Franx, M., Illingworth, G. D., & Forbes, D. A. 1997, *ApJ*, 481, 710
- Carollo, C. M., Stiavelli, M., & Mack, J. 1998, *AJ*, 116, 68
- Carollo, C. M., Stiavelli, M., Seigar, M., de Zeeuw, P. T., & Dejonghe, H. 2002, *AJ*, 123, 159
- Cavaliere, A. & Vittorini, V. 2002, *ApJ*, 570, 114
- Chokshi, A. & Turner, E. L. 1992, *MNRAS*, 259, 421
- de Jong, R. S. 1996, *A&A*, 313, 377 (IV)
- de Vaucouleurs, G., de Vaucouleurs, A., Corwin, J. R., Buta, R. J., Paturel, G., & Fouque, P. 1991, *Third reference catalogue of Bright galaxies*, (New York: Springer-Verlag)
- Devereux, N., Ford, H., & Jacoby, G. 1997, *ApJ*, 481, L71

- Ferrarese, L., Ford, H. C., & Jaffe, W. 1996, *ApJ*, 470, 444
- Ferrarese, L. & Merritt, D. 2000, *ApJ*, 539, L9
- Ford, H. C., Tsvetanov, Z. I., Ferrarese, L., & Jaffe, W. 1998, in *The Central Regions of the Galaxy and Galaxies*, ed. Y. Sofue (Dordrecht: Kluwer), 377
- Ford, H. C., et al. 1994, *ApJ*, 435, L27
- Gebhardt, K. et al. 2000, *ApJ*, 539, L13
- Genzel, R., Pichon, C., Eckart, A., Gerhard, O. E., & Ott, T. 2000, *MNRAS*, 317, 348
- Giovanelli, R. & Haynes, M. P. 2002, *ApJ*, 571, L107
- Greenhill, L. J., Moran, J. M., & Herrnstein, J. R. 1997, *ApJ*, 481, L23
- Harms, R. J., et al. 1994, *ApJ*, 435, L35
- Ho, L. C., Filippenko, A. V., & Sargent, W. L. W. 1997, *ApJ*, 487, 568
- Ho, L. C., Sarzi, M., Rix, H., Shields, J. C., Rudnick, G., Filippenko, A. V., & Barth, A. J. 2002, *PASP*, 114, 137
- Kinney, A. L., Calzetti, D., Bohlin, R. C., McQuade, K., Storchi-Bergmann, T., & Schmitt, H. R. 1996, *ApJ*, 467, 38
- Knapen, J. H., Beckman, J. E., Heller, C. H., Shlosman, I., & de Jong, R. S. 1995, *ApJ*, 454, 623
- Kormendy, J., & Richstone, D. 1995, *ARA&A*, 33, 581
- Kormendy, J., et al. 1996, *ApJ*, 459, L57
- Kormendy, J., & Gebhardt, K. 2001, in *20th Texas Symposium on Relativistic Astrophysics*, eds. J. C. Wheeler and H. Martel (Melville, NY: AIP), 363
- Krist, J. & Hook, R. 1999, *The Tiny Tim User's Guide* (Baltimore: STScI)
- Jaffe, W., Ford, H., Ferrarese, L., van den Bosch, F., & O'Connell, R. W. 1996, *ApJ*, 460, 214
- Leitherer, C., et al. 2001, "STIS Instrument Handbook", Version 5.1, (Baltimore: STScI).
- Leitherer, C. et al. 1999, *ApJS*, 123, 3
- Lynden-Bell, D. 1969, *Nature*, 223, 690
- Macchetto, F., Marconi, A., Axon, D. J., Capetti, A., Sparks, W., & Crane, P. 1997, *ApJ*, 489, 579
- Maciejewski, W. & Binney, J. 2001, *MNRAS*, 323, 831
- Maiolino, R., & Rieke, G. H. 1995, *ApJ*, 454, 95
- Maraston, C. 1998, *MNRAS*, 300, 872
- Marconi, A., & Salvati M., N. 2002, in *Issues in Unification of Active Galactic Nuclei*, eds. R. Maiolino, A. Marconi and N. Nagar (San Francisco: ASP), 217
- Marconi, A., Capetti, A., Axon, D. J., Koekemoer, A., Macchetto, D., & Schreier, E. J. 2001, *ApJ*, 549, 915
- Marconi, A., Schreier, E. J., Koekemoer, A., Capetti, A., Axon, D., Macchetto, D., & Caon, N. 2000, *ApJ*, 528, 276
- McLure, R. J., & Dunlop, J. S. 2002, *MNRAS*, 331, 795
- Merritt, D., & Ferrarese, L. 2001, *ApJ*, 547, 140
- Merritt, D. & Ferrarese, L. 2001, in *The Central Kiloparsec of Starbursts and AGN*, eds. J. H. Knapen et al. (San Francisco: ASP), 335
- Merritt, D. 1997, *AJ*, 114, 228
- Miyoshi, M., Moran, J., Herrnstein, J., Greenhill, L., Nakai, N., Diamond, P., & Inoue, M. 1995, *Nature*, 373, 127
- Moriondo, G., Giovanardi, C., & Hunt, L. K. 1998, *A&A*, 339, 409
- Osterbrock, D. E., 1989, *Astrophysics of Gaseous Nebulae and Active Galactic Nuclei*, (Mill Valley, CA: University Science Books)
- Panagia, N. 1973, *AJ*, 78, 929

- Press, W. H., Teukolsky, S. A., Vetterling, W. T., & Flannery, B. P. 1992, *Numerical Recipes in C. The Art of Scientific computing*, (Cambridge: University Press), 2nd edition.
- Pryor, C., & Meylan, G. 1993, in *Structure and Dynamics of Globular Clusters*, eds. S. G. Djorgovski and G. Meylan (San Francisco: ASP), 357
- Richstone, D. 1998, *BAAS*, 30, 1140
- Sakamoto, K., Okumura, S. K., Ishizuki, S., & Scoville, N. Z. 1999, *ApJS*, 124, 403
- Salpeter, E. E. 1955, *ApJ*, 121, 161
- Scalo, J. M. 1986, *Fundamentals of Cosmic Physics*, 11, 1
- Schreier, E. J., et al. 1998, *ApJ*, 499, L143
- Shaw, M., Axon, D., Probst, R., & Gatley, I. 1995, *MNRAS*, 274, 369
- Silk, J., & Rees, M. J. 1998, *A&A*, 331, L1
- Simien, F., & de Vaucouleurs, G. 1986, *ApJ*, 302, 564
- Sołtan, A. 1982, *MNRAS*, 200, 115
- Statler, T. S. 1987, *ApJ*, 321, 113
- Tremaine, S. et al. 2002, *ApJ*, 574, 740
- van der Marel, R. P., & van den Bosch, F. C. 1998, *AJ*, 116, 2220
- van der Marel, R. P., Cretton, N., de Zeeuw, P. T., & Rix, H. 1998, *ApJ*, 493, 613
- Verdoes Kleijn, G. A., van der Marel, R. P., Carollo, C. M., & de Zeeuw, P. T. 2000, *AJ*, 120, 1221
- Whitmore, B. 1995, in *Calibrating Hubble Space Telescope. Post Servicing Mission*, eds. A. Koratkar and C. Leitherer (Baltimore: STScI), 269
- Wilkins, T. W., & Axon, D. J. 1992, in *Astronomical Data Analysis Software and Systems I*, eds. D. M. Worrall, C. Biemesderfer, & J. Barnes (San Francisco: ASP), 427
- Winge, C., Axon, D. J., Macchetto, F. D., Capetti, A., & Marconi, A. 1999, *ApJ*, 519, 134

### A. Deriving the luminosity density of the stars from the observed surface brightness profile

The stellar luminosity density can be inferred by inverting the observed observed surface brightness profiles. Following van der Marel & van den Bosch (1998) we assume an oblate spheroidal density distribution which we parameterize as:

$$\rho(m) = \rho_0 \left( \frac{m}{r_b} \right)^{-\alpha} \left( 1 + \left( \frac{m}{r_b} \right)^2 \right)^{-\beta} \quad (\text{A1})$$

$m$  is defined as  $m^2 = x^2 + y^2 + z^2/q^2$ , where  $xyz$  is a reference system with the  $xy$  plane corresponding to the principal plane of the potential.  $q$  is the intrinsic axial ratio of the mass distribution. If  $\Upsilon$  is the mass-to-light ratio, the observed surface brightness distribution is given by<sup>14</sup>:

$$\Sigma = \frac{1}{4\pi\Upsilon} \int_{-\infty}^{+\infty} \rho ds \quad (\text{A2})$$

where the integration is performed along the line of sight. It can be shown that

$$\Sigma(m') = \frac{1}{4\pi\Upsilon} \frac{q}{q'} \int_{m'^2}^{+\infty} \frac{\rho(m^2) dm^2}{\sqrt{(m^2 - m'^2)}} \quad (\text{A3})$$

where  $m'^2 = x'^2 + y'^2/q'^2$  and  $x'y'$  is a reference system on the sky, with the  $x'$  axis aligned along the apparent major axis.  $q'$  is the observed axial ratio of the isophotes which is related to the intrinsic axial ratio of the mass distribution by  $q'^2 = \cos^2 i + q^2 \sin^2 i$ , where  $i$  is the inclination of the line of sight ( $i = 90^\circ$  is the edge-on case). The observed surface brightness results from the convolution of  $\Sigma$  with the *point spread function*  $P$  of the system (i.e. telescope and optics) and the detector pixels:

$$\Sigma_{\text{app}}(X, Y) = \int_{X-\Delta X}^{X+\Delta X} \int_{Y-\Delta Y}^{Y+\Delta Y} \left[ \int_{-\infty}^{+\infty} \int_{-\infty}^{+\infty} \Sigma_{\text{true}}(x, y) P(x' - x, y' - y) dx dy \right] \frac{dx' dy'}{4\Delta X \Delta Y} \quad (\text{A4})$$

where  $X, Y$  is the centre of an aperture with size  $2\Delta X \times 2\Delta Y$ . The integration on  $dx' dy'$  can be directly carried out on the PSF  $P$  which is described by a sum of gaussians:

$$P(x, y) = \frac{1}{N_K} \sum_{i=1}^N k_i \exp \left( -\frac{x^2 + y^2}{2\sigma_i^2} \right) \quad (\text{A5})$$

with  $N_K = \sum_{i=1}^N 2\pi\sigma_i^2 k_i$ . Then  $\Sigma_{\text{app}}$  is given by

$$\Sigma_{\text{app}}(X, Y) = \int_{-\infty}^{+\infty} \int_{-\infty}^{+\infty} \Sigma(x, y)_{\text{true}} \mathcal{K}(X - \Delta X - x, X + \Delta X - x; Y - \Delta Y - y, Y + \Delta Y - y) \frac{dx dy}{4\Delta X \Delta Y} \quad (\text{A6})$$

where  $\mathcal{K}$  is the convolution kernel:

$$\mathcal{K}(X_1, X_2; Y_1, Y_2) = \frac{1}{N_K} \sum_{i=1}^N 2\pi\sigma_i^2 \frac{k_i}{4} \left[ \mathcal{E} \left( \frac{X_1}{\sigma_i \sqrt{2}} \right) - \mathcal{E} \left( \frac{X_2}{\sigma_i \sqrt{2}} \right) \right] \left[ \mathcal{E} \left( \frac{Y_1}{\sigma_i \sqrt{2}} \right) - \mathcal{E} \left( \frac{Y_2}{\sigma_i \sqrt{2}} \right) \right] \quad (\text{A7})$$

where  $\mathcal{E}$  is the complementary error function. The integration is then carried out numerically using the Gauss Legendre approximation.

<sup>14</sup>Note the  $1/4\pi$  factor. This derives from the fact that  $\rho/V$  is a density (luminosity per unit volume) and  $\Sigma$  is a surface brightness (luminosity per unit area per unit solid angle).

The best fitting model is determined by minimizing the reduced  $\chi_{\text{red}}^2$  defined as:

$$\chi_{\text{red}}^2 = \frac{1}{N_d} \sum_{i=1}^N \left( \frac{\log \Sigma_i - \log \Sigma_m(r_i, \delta r_i; p_1, \dots, p_m)}{\delta \log \Sigma_i} \right)^2 \quad (\text{A8})$$

$$(\text{A9})$$

where  $i = 1, \dots, N$  indicates a data point with surface brightness  $\Sigma_i \pm \delta \Sigma_i$  at radius  $r_i$ .  $\Sigma_m(r_i, \delta r_i; p_1, \dots, p_m)$  is the model surface brightness, averaged over radii  $r_i - \delta r_i \leq r \leq r_i + \delta r_i$ , which is a function of  $m$  free parameters  $p_1, \dots, p_m$ .  $N_d = N - m$  is the number of degrees of freedom. The  $\chi_{\text{red}}^2$  is minimized to determine the  $m$  free parameters using the downhill simplex algorithm by Press et al. (1992).

When the mass density has been determined as described above, the circular velocity in the principal plane is given by the relation (e.g. Binney & Tremaine 1987):

$$V_c^2(r) = 4\pi G q^2 \int_0^r \frac{\rho(m^2) m^2 dm}{\sqrt{r^2 - m^2 e^2}} \quad (\text{A10})$$

where  $e$  is the eccentricity related to  $q$  by  $q^2 = 1 - e^2$ . Similarly the mass enclosed within the homoeoid defined by  $m < m_o$  is

$$M(m_o) = 4\pi q \int_0^{m_o} \rho(m^2) m^2 dm \quad (\text{A11})$$

## B. The rotation curve model

The velocity field along the line of sight,  $\bar{v}$ , can be easily computed in the case of a circularly rotating thin disk. Let  $XY$  be a reference frame in the plane of the sky with  $Y$  axis fixed along the direction given by the slit position (hereafter called the slit reference frame). Consider a reference frame  $X_d Y_d$  in the sky with the  $X_d$  axis aligned along the disk line of nodes and the origin coincident with the disk centre (hereafter called the “disk reference frame”, see Figure 20). The origin of  $XY$  is chosen in such a way that the disk center has coordinates  $x = b$  and  $y = 0$  in the slit reference frame. Then a given disk point  $P$  with coordinates  $(x, y)$  in the slit reference frame has coordinates  $(x_d, y_d)$  in the disk reference frame given by

$$\begin{aligned} x_d &= (x - b) \sin \theta + y \cos \theta \\ y_d &= -(x - b) \cos \theta + y \sin \theta \end{aligned} \quad (\text{B1})$$

If the disk has an inclination angle  $i$  ( $i = 0$  in the face-on case), then  $P$  is at the disk radius  $r$  given by

$$r^2 = x_d^2 + \left( \frac{y_d}{\cos i} \right)^2 \quad (\text{B2})$$

The circular velocity of  $P$ , in the case of a spherical mass distribution, is then given by

$$V_c(r) = \left| r \frac{d\Phi}{dr} \right|^{\frac{1}{2}} = \left( \frac{GM(r)}{r} \right)^{\frac{1}{2}} \quad (\text{B3})$$

where  $M(r)$  is the enclosed mass at radius  $r$ , a constant value  $M_{\text{BH}}$  in case of a point mass. In the case of an oblate spheroidal mass distribution,  $V_c(r)$  is given by Equation A10.

The velocity component along the line of sight is finally given by

$$\bar{v} = V_{\text{sys}} - V_c(r) \sin i \frac{x_d}{r} = V_{\text{sys}} - (GM_{\text{BH}})^{0.5} \sin i \frac{x_d}{r^{1.5}} \quad (\text{B4})$$

with the latter expression describing the simple case of a point mass  $M_{\text{BH}}$ .

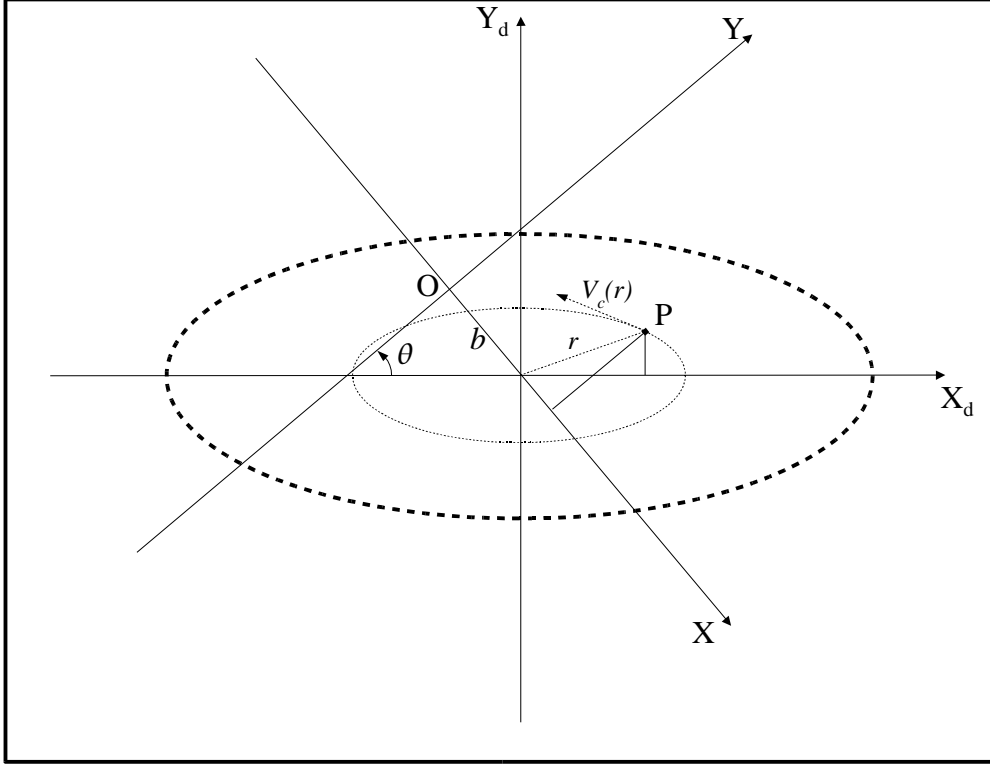


Fig. 20.— Geometry of the disk.

This velocity field  $\bar{v}$  has to be convolved with the instrumental response in order to simulate the observed quantities. Below we show how can this be done for any velocity field  $\bar{v}$ .

Consider again the reference frame  $XY$  in the plane of the sky defined above. The light distribution can be written as

$$\Phi(x', y', v) = I(x', y') \phi(v - \bar{v}), \quad (\text{B5})$$

where  $I(x', y')$  is the total intensity at the point  $(x', y')$ , and  $\phi(v - \bar{v})$  is the intrinsic line profile centered at the velocity along the line of sight  $\bar{v}(x', y')$ . After passing through the telescope, the light gets convolved with the instrumental PSF  $P(x - x', y - y')$ , and at point  $(x, y)$  in the focal plane the light distribution is described by

$$\Phi(x, y, v) = \int \int_{-\infty}^{+\infty} dx' dy' I(x', y') \phi(v - \bar{v}) P(x - x', y - y'). \quad (\text{B6})$$

As already defined, the slit in the focal plane is aligned along the  $Y$  axis and let its center cross the  $X$  axis at  $x_0$ . Let the slit width be  $2\Delta x$ . Past the slit, the light falls into the detector plane, where the spatial coordinate  $x$  and the velocity  $v$  are combined into one single detector coordinate  $w = v + k(x - x_0)$ , which we identify with the *observed* velocity (we denote it  $w$  here in contrast to the intrinsic velocity denoted by  $v$ ). Here, the coefficient  $k$  is given by  $\mu\Delta w/\Delta y$  where  $\mu$ , the anamorphic magnification, accounts for the different scales on the dispersion and slit directions. In the case of STIS, the scale along the slit is  $0''.05071$  and along dispersion is  $0''.05477$ , thus  $\mu = 1.080$  (Bowers & Baum 1998). The light distribution in the detector plane,  $\Psi(w, y)$ , is calculated by ousting  $v$ , and integrating the light contribution across the slit

$$\Psi(w, y) = \int_{x_0 - \Delta x}^{x_0 + \Delta x} dx \Phi(x, y, w - k(x - x_0))$$



$$= \int_{x_0-\Delta x}^{x_0+\Delta x} dx \int_{-\infty}^{+\infty} dx' dy' \phi[w - \bar{v}(x', y') - k(x - x_0)] I(x', y') P(x - x', y - y'). \quad (\text{B7})$$

Note the component  $k(x - x_0)$  in the velocity profile, which is the “spurious” velocity for light entering off from the slit center. Properties of thus defined two-dimensional light distribution with the spurious velocity shift were investigated in detail by Maciejewski & Binney (2001).

The detector integrates over finite pixel sizes therefore we calculate the expected line fluxes, average velocities and widths for the line profile that is obtained by integrating the light distribution on the detector plane  $\Psi(w, y)$  over the width  $2\Delta y$  of the  $j^{\text{th}}$  pixel along the slit, and convolving it with the shape of the pixel in the dispersion direction: a top-hat of width  $2\Delta w$ . Thus the expected line profile in the detector is

$$\tilde{\Psi}_j(w) = \int_{y_j-\Delta y}^{y_j+\Delta y} dy \int_{w-\Delta w}^{w+\Delta w} dw \Psi(w', y), \quad (\text{B8})$$

where the  $j^{\text{th}}$  pixel has the coordinate  $y_j$  along the slit. Note that the observed intensities are measured at discrete values of  $w$  corresponding to the pixel centers. In order to calculate the expected line fluxes, average velocities and widths, one has to evaluate moments of  $\tilde{\Psi}_j(w)$ :

$$\int_{-\infty}^{+\infty} dw w^n \tilde{\Psi}_j(w) = \int_{y_j-\Delta y}^{y_j+\Delta y} dy \int_{x_0-\Delta x}^{x_0+\Delta x} dx \int_{-\infty}^{+\infty} dx' dy' \mathcal{P} \int_{-\infty}^{+\infty} dw w^n \int_{w-\Delta w}^{w+\Delta w} dw' \phi(w' - w_0) \quad (\text{B9})$$

where we used abbreviations  $\mathcal{P} = I(x', y')P(x - x', y - y')$  and  $w_0 = \bar{v}(x', y') + k(x - x_0)$ . The last two integrals can be simplified by inverting the order of integration:

$$\begin{aligned} \int_{-\infty}^{+\infty} dw w^n \int_{w-\Delta w}^{w+\Delta w} dw' \phi(w' - w_0) &= \int_{-\infty}^{+\infty} dw dw' w^n \phi(w' - w_0) H(w - w') = \\ \int_{-\infty}^{+\infty} dw \phi(w - w_0) \int_{w-\Delta w}^{w+\Delta w} dw' w'^n &= \int_{-\infty}^{+\infty} dw \phi(w - w_0) \frac{(w + \Delta w)^{n+1} - (w - \Delta w)^{n+1}}{n+1} \end{aligned}$$

where  $H(w - w')$  is 1 for  $|w - w'| < \Delta w$  and 0 otherwise. This leads to the following formulae for the moments of  $\tilde{\Psi}_j(w)$ :

$$\int_{-\infty}^{+\infty} \tilde{\Psi}_j(w) dw = 2\Delta w \int_{x_0-\Delta x}^{x_0+\Delta x} dx \int_{y_j-\Delta y}^{y_j+\Delta y} dy \int_{-\infty}^{+\infty} dx' dy' \mathcal{P} \quad (\text{B10})$$

$$\int_{-\infty}^{+\infty} w \tilde{\Psi}_j(w) dw = 2\Delta w \int_{x_0-\Delta x}^{x_0+\Delta x} dx \int_{y_j-\Delta y}^{y_j+\Delta y} dy \int_{-\infty}^{+\infty} dx' dy' w_0 \mathcal{P} \quad (\text{B11})$$

$$\int_{-\infty}^{+\infty} w^2 \tilde{\Psi}_j(w) dw = 2\Delta w \int_{x_0-\Delta x}^{x_0+\Delta x} dx \int_{y_j-\Delta y}^{y_j+\Delta y} dy \int_{-\infty}^{+\infty} dx' dy' (w_0^2 + \frac{(\Delta w)^2}{3} + \sigma^2) \mathcal{P} \quad (\text{B12})$$

To obtain them, we assumed that the intrinsic velocity profile  $\phi(v)$  is bound and symmetric, i.e.

$$\int_{-\infty}^{+\infty} \phi(v) dv = 1 \quad \int_{-\infty}^{+\infty} v \phi(v) dv = 0 \quad \int_{-\infty}^{+\infty} v^2 \phi(v) dv = \sigma^2$$

where  $\sigma^2$  is the intrinsic velocity dispersion.

Equations B10, B11 and B12 can be used to compute the expected line fluxes, average velocities and widths. For example, in the most simple case of a constant line intensity  $I = \text{const}$ , and velocity field  $\bar{v} = \text{const}$ , one can write:

$$\begin{aligned}\langle v_j \rangle &= \frac{\int_{-\infty}^{+\infty} w \tilde{\Psi}_j(w) dw}{\int_{-\infty}^{+\infty} \tilde{\Psi}_j(w) dw} = \bar{v} \\ \langle v_j^2 \rangle &= \frac{\int_{-\infty}^{+\infty} w^2 \tilde{\Psi}_j(w) dw}{\int_{-\infty}^{+\infty} \tilde{\Psi}_j(w) dw} = \bar{v}^2 + \sigma^2 + \frac{(\Delta w)^2}{3} + \frac{(k\Delta x)^2}{3}.\end{aligned}\quad (\text{B13})$$

Then the expected velocity dispersion, given by  $\sigma_j^2 = \langle v_j^2 \rangle - \langle v_j \rangle^2$ , is, understandably, larger than the intrinsic velocity dispersion  $\sigma$ . This is due to the convolution with the pixel size and slit width, which add quadratically. However, note that while  $\Delta w$  and  $\sigma$  enter the integral (B12) as constants,  $w_0$  is a linear combination of the spurious velocity shift, and the intrinsic velocity. These two contributions can cancel, resulting in the expected line profile being broadened by the pixel size only, and not by the width of the slit. This implies that the wide slit can probe the disk on the scale of the pixel size rather than the slit width. Maciejewski & Binney (2001) explore consequences of this finding.

In order to compute the model given by Equations B10, B11, and B12, we create a grid in  $x$  and  $y$  with sampling given by  $\sigma_{\text{PSF}}/n$ . Here,  $\sigma_{\text{PSF}}$  is the spatial r.m.s. of the point spread function (PSF) and  $n$  is the subsampling factor. We have verified that the optimal subsampling factor used is  $n = 3$  since larger values do not produce any appreciable differences in the final results. The PSF used is the one generated by TinyTim (V6.0, Krist & Hook 1999) at 6700Å. Convolution with the PSF is done using the *Fast Fourier Transform* algorithm Press et al. (1992). Following Barth et al. (2001) we have also introduced the CCD scattering function Leitherer et al. (2001) but, as already noticed by them, it does not have any appreciable effect in the final results.

We compare models to the observed spectrum, which is essentially an array of intensities  $\Psi_{ij}$ , after the observed line profile is derived in the following way: to the sequence of intensities  $\Psi_{ij}$  for a given row  $j$  along the slit, we fit a baseline, and a continuous analytical function  $\tilde{\Psi}_j(w)^{\text{obs}}$ , which we interpret as the observed equivalent of the expected line profile  $\tilde{\Psi}_j(w)$  (eq.B8). The best fitting model is determined by minimizing the reduced  $\chi_{\text{red}}^2$  defined as:

$$\chi_{\text{red}}^2 = \frac{1}{N_d} \sum_{k=1}^3 \sum_{j=1}^{N_k} \left[ \left( \frac{v_{kj} - \langle v_j \rangle_k(p_1, \dots, p_m)}{\delta v_{kj}} \right)^2 + \left( \frac{W_{kj} - \langle W_j \rangle_k(p_1, \dots, p_m)}{\delta W_{kj}} \right)^2 \right] \quad (\text{B14})$$

where the index  $k = 1, 3$  indicates the slit position, and  $j = 1, N_k$  counts pixels along the slit. Here, the characteristics of the model are as follows. The velocity in the  $j^{\text{th}}$  row along the slit  $\langle v_j \rangle_k$ , and the FWHM of the velocity profile  $\langle W_j \rangle_k$ , are calculated directly from equations (B13), now clearly for variable intensity and velocity field. They both are functions of  $m$  free parameters  $p_1, \dots, p_m$ , which are determined by  $\chi_{\text{red}}^2$  minimization. The FWHM is calculated from the expected velocity dispersion  $\sigma_j$  after assuming a Gaussian line profile. The observed velocities ( $v_{ki} \pm \delta v_{ki}$ ), and velocity dispersions ( $W_{ki} \pm \delta W_{ki}$ ) are also derived from equations (B13), but after  $\tilde{\Psi}_j(w)$  has been replaced by  $\tilde{\Psi}_j(w)^{\text{obs}}$  defined above.  $N_d = \sum_{k=1}^3 2N_k - m$  is the number of degrees of freedom.

The  $\chi_{\text{red}}^2$  is minimized to determine the  $m$  free parameters using the downhill simplex algorithm by Press et al. (1992). In order to apply statistical methods when  $\chi_{\text{red}}^2$  is much larger than 1, we follow Barth et al. (2001) and rescale errors as:

$$(\delta v'_{ki})^2 = \delta v_{ki}^2 + \delta V^2 \quad (\text{B15})$$

where  $\delta V$  is a “systematic” error determined such that the resulting  $\chi_c^2$  of the “best” model is 1. The fits presented in this paper have  $\chi_{\text{red}}^2 \sim 1$  and the error rescaling was not performed.